



HAL
open science

Review of ” Universal ” Rules Governing Bone Composition, Organization, and Elasticity Across Organizational Hierarchies

Viktorija Vass, Claire Morin, Stefan Scheiner, Christian Hellmich

► **To cite this version:**

Viktorija Vass, Claire Morin, Stefan Scheiner, Christian Hellmich. Review of ” Universal ” Rules Governing Bone Composition, Organization, and Elasticity Across Organizational Hierarchies. Multiscale Mechanobiology of Bone Remodeling and Adaptation, 2018. hal-01671668

HAL Id: hal-01671668

<https://hal.science/hal-01671668>

Submitted on 22 Dec 2017

HAL is a multi-disciplinary open access archive for the deposit and dissemination of scientific research documents, whether they are published or not. The documents may come from teaching and research institutions in France or abroad, or from public or private research centers.

L'archive ouverte pluridisciplinaire **HAL**, est destinée au dépôt et à la diffusion de documents scientifiques de niveau recherche, publiés ou non, émanant des établissements d'enseignement et de recherche français ou étrangers, des laboratoires publics ou privés.

Metadata of the chapter that will be visualized in SpringerLink

Book Title	Multiscale Mechanobiology of Bone Remodeling and Adaptation	
Series Title		
Chapter Title	Review of “Universal” Rules Governing Bone Composition, Organization, and Elasticity Across Organizational Hierarchies	
Copyright Year	2018	
Copyright HolderName	CISM International Centre for Mechanical Sciences	
Author	Family Name	Vass
	Particle	
	Given Name	Viktoria
	Prefix	
	Suffix	
	Division	Institute for Mechanics of Materials and Structures
	Organization	TU Wien – Vienna University of Technology
	Address	Vienna, Austria
	Email	
Author	Family Name	Morin
	Particle	
	Given Name	Claire
	Prefix	
	Suffix	
	Division	Ecole Nationale Supérieure des Mines de Saint Etienne
	Organization	CIS-EMSE, SAINBIOSE
	Address	F-42023, Saint-Etienne, France
	Division	
	Organization	INSERM U1059, SAINBIOSE
	Address	F-42023, Saint-Etienne, France
	Email	claire.morin@emse.fr
Author	Family Name	Scheiner
	Particle	
	Given Name	Stefan
	Prefix	
	Suffix	
	Division	Institute for Mechanics of Materials and Structures
	Organization	TU Wien – Vienna University of Technology
	Address	Vienna, Austria
	Email	
Corresponding Author	Family Name	Hellmich
	Particle	
	Given Name	Christian
	Prefix	
	Suffix	

Division	Institute for Mechanics of Materials and Structures
Organization	TU Wien – Vienna University of Technology
Address	Vienna, Austria
Email	christian.hellmich@tuwien.ac.at

Abstract

“Universal” organizational patterns in bone are reviewed and presented, in terms of mathematically expressed rules concerning the composition and elasticity of a large variety of tissues. Firstly, experimental data sets gained from dehydration-demineralization tests, dehydration-deorganization tests, and dehydration-ashing tests are thoroughly analyzed. On this basis, bilinear relations can be identified, between the mass density of the extracellular bone matrix on the one hand, and the apparent mass densities of its basic constituents (water, hydroxyapatite, and organic matter), on the other hand. Secondly, the question as to how hydroxyapatite is distributed in bone tissue is addressed. To that end, mass and volume measurements gained from wet, dehydrated, and demineralized tissue samples, as well as optical densities provided by transmission electron microscopy, are studied, confirming a rule on how the mineral is partitioned between fibrillar and extrafibrillar spaces in the ultrastructure of bone. Thirdly, a swelling rule for hydrating collagen is validated through processing of experimental data from X-ray diffraction, vacuum drying, and mass measurements, quantifying the change of the bone tissue composition upon hydration. And fourthly, application of the mass conservation law to extracellular bone matrix considered as closed thermodynamic system, allows for studying the change of bone tissue composition during mineralization. Finally, these compositional rules, which are shown to be “universally” valid throughout the vertebrate kingdom, enter a micromechanical homogenization scheme for upscaling the experimentally accessible elastic properties of the elementary mechanical building blocks of bone (hydroxyapatite minerals, type I collagen, and water with non-collageneous organics) to the macroscopic scale of cortical and trabecular bone.

Keywords
(separated by '-')

Bone mechanics - Elasticity - Strength - Micromechanics - Multiscale modeling

Review of “Universal” Rules Governing Bone Composition, Organization, and Elasticity Across Organizational Hierarchies

Viktoria Vass, Claire Morin, Stefan Scheiner and Christian Hellmich

1 **Abstract** “Universal” organizational patterns in bone are reviewed and presented,
2 in terms of mathematically expressed rules concerning the composition and elasticity
3 of a large variety of tissues. Firstly, experimental data sets gained from dehydration-
4 demineralization tests, dehydration-deorganization tests, and dehydration-ashing
5 tests are thoroughly analyzed. On this basis, bilinear relations can be identified,
6 between the mass density of the extracellular bone matrix on the one hand, and the
7 apparent mass densities of its basic constituents (water, hydroxyapatite, and organic
8 matter), on the other hand. Secondly, the question as to how hydroxyapatite is dis-
9 tributed in bone tissue is addressed. To that end, mass and volume measurements
10 gained from wet, dehydrated, and demineralized tissue samples, as well as optical
11 densities provided by transmission electron microscopy, are studied, confirming a
12 rule on how the mineral is partitioned between fibrillar and extrafibrillar spaces in
13 the ultrastructure of bone. Thirdly, a swelling rule for hydrating collagen is validated
14 through processing of experimental data from X-ray diffraction, vacuum drying, and
15 mass measurements, quantifying the change of the bone tissue composition upon
16 hydration. And fourthly, application of the mass conservation law to extracellular
17 bone matrix considered as closed thermodynamic system, allows for studying the
18 change of bone tissue composition during mineralization. Finally, these composi-
19 tional rules, which are shown to be “universally” valid throughout the vertebrate
20 kingdom, enter a micromechanical homogenization scheme for upscaling the exper-
21 imentally accessible elastic properties of the elementary mechanical building blocks

V. Vass · S. Scheiner · C. Hellmich (✉)
Institute for Mechanics of Materials and Structures,
TU Wien – Vienna University of Technology, Vienna, Austria
e-mail: christian.hellmich@tuwien.ac.at

C. Morin
Ecole Nationale Supérieure des Mines de Saint Etienne,
CIS-EMSE, SAINBIOSE, F-42023 Saint-Etienne, France
e-mail: claire.morin@emse.fr

C. Morin
INSERM U1059, SAINBIOSE, F-42023 Saint-Etienne, France

© CISM International Centre for Mechanical Sciences 2017
P. Pivonka (ed.), *Multiscale Mechanobiology of Bone Remodeling
and Adaptation*, CISM International Centre for Mechanical Sciences 578,
DOI 10.1007/978-3-319-58845-2_4

1

22 of bone (hydroxyapatite minerals, type I collagen, and water with non-collagenous
 23 organics) to the macroscopic scale of cortical and trabecular bone.

24 **Keywords** Bone mechanics · Elasticity · Strength · Micromechanics · Multiscale
 25 modeling

26 **Nomenclature**

27	\mathbb{A}	fourth-order strain concentration tensor
28	\mathbb{c}, \mathbb{C}	fourth-order elasticity tensor at the “microscopic” and “macroscopic” 29 scale, respectively
30	d	lateral/equatorial diffraction spacing
31	ℓ	characteristic length of the heterogeneities inside the RVE
32	div	divergence (mathematical operator)
33	\mathbb{D}	fourth-order compliance tensor
34	D_{ijkl}	component $ijkl$ of tensor \mathbb{D}
35	D	axial diffraction spacing / axial macroperiod
36	$d\mathbf{x}_i$	line element along the principal direction i
37	E	Young’s modulus
38	\mathbf{E}	macroscopic strain tensor
39	f	volume fraction
40	g	gravitational acceleration
41	GRAD	gradient operator at the structure scale
42	\mathbb{I}	fourth-order identity tensor
43	J	Jacobian, quantifying volume change during hydration process
44	k	elastic bulk modulus
45	ℓ	characteristic length of the RVE
46	\mathcal{L}	characteristic length of the structure built up by RVEs, or of its loading
47	M	mass concerning a millimeter-sized bone sample
48	\min	minimum value (mathematical operator)
49	N_r	number of phases
50	\mathbf{n}	outwardly pointing vector normal to a surface element of an RVE
51	\mathbb{P}_r^s	fourth-order Hill tensor of inclusion with shape r (or phase r) embedded 52 in matrix with stiffness \mathbb{C}_r (or \mathbb{C}^0 if $s = 0$), or with symmetry property s 53 otherwise
54	\mathcal{R}	water-to-organic mass ratio
55	RVE	Representative Volume Element
56	\mathbf{T}	traction vector
57	v	velocity
58	V	volume quantity concerning a millimeter-sized bone sample
59	W	weight quantity concerning a millimeter-sized bone sample
60	\mathcal{W}	work
61	WF	weight fraction
62	\mathbf{x}	location vector
63	β	proportionality constant between extrafibrillar space and fibrillar space 64 increase during hydration

65	∂V	boundary of volume V
66	$\boldsymbol{\varepsilon}$	microscopic strain field
67	$\boldsymbol{\varepsilon}_r$	average (micro-)strain in phase r
68	λ_i	principal stretch in direction i
69	μ	elastic shear modulus
70	ϕ	relative mineral portion in extrafibrillar space
71	ρ	mass density
72	$\boldsymbol{\sigma}$	microscopic stress field
73	$\boldsymbol{\sigma}_r$	average (micro-)stress in phase r
74	$\boldsymbol{\Sigma}$	macroscopic stress tensor
75	$\boldsymbol{\xi}$	displacement field

76 *Operators*

77	$\langle \langle \cdot \rangle \rangle$	average of quantity (\cdot) over the volume of the RVE
78	:	double contraction
79	.	simple contraction (dot product)

80 *Subscripts*

81	air	measured in air
82	ash	...of ash
83	ax	...in axial direction
84	can	...of canalicular porosity
85	col	...of collagen
86	dev	deviatoric part
87	dry	in dry state
88	excol	...of extracollageneous space
89	exfib	...of extrafibrillar space
90	fib	...of fibril
91	fl	...of ionic fluid
92	HA	...of hydroxyapatite
93	H ₂ O	...of water
94	i	...of constituent i
95	lac	...of lacunar porosity
96	liquid	...of liquid used for the Archimedes' tests
97	m	...of the matrix phase
98	max	maximum value (typically related to full saturation)
99	org	...of organic matter
100	r	...of phase r
101	<i>RVE</i>	...of the Representative Volume Element
102	sub	measured when submerged in water
103	tr	...in transverse direction
104	vas	...of vascular porosity
105	vol	volumetric part
106	w	...in wet (hydrated) state
107	wetcol	...of wet collagen

108	0	at the time of osteoid deposition
109	1, 2	...in transverse direction
110	3	...in axial direction
111	∞	...in fully mineralized state
112	μpor	...of microporosity

113 *Superscripts*

114	col	...per volume of molecular collagen
115	cort	...per volume of cortical space
116	dry	...per volume of dry bone tissue
117	dh	...of partially dehydrated tissue
118	excel	...per volume of extracellular space
119	excol	...per volume of extracollageneous space
120	exfib	...per volume of extrafibrillar space
121	exp	experimental value
122	ext	...of external forces acting on the RVE
123	exvas	...per volume of extravascular space
124	fib	...per volume of fibrillar space
125	fibsat	at fibrillar saturation limit
126	hom	homogenized
127	int	...of internal forces acting within the RVE
128	imsat	at intermolecular pore saturation limit
129	pred	model-predicted value
130	μ	...of a millimeter-sized bone sample
131	0	related to the matrix phase in the auxiliary Eshelby problem

132 **1 Introduction**

133 Many tasks in the diverse field of biomedical engineering involve ensuring the
 134 mechanical integrity of structures made up by biological tissues. The mechanical
 135 integrity of structures depends on the mechanical loading to which they are sub-
 136 jected, on the specific shapes of the structures (i.e. of the organs), and last, but not
 137 least, on the mechanical properties of the materials (i.e. of the biological tissues) mak-
 138 ing up the structures. The aforementioned tissue properties, changing in time and
 139 space across the organs, depend on tissue composition and on the micro- and nanos-
 140 tructures within a piece of tissue. The present contribution reviews rigorously derived
 141 mathematical relations describing corresponding structure-property relations.

142 This topic is closely linked to the question on whether there are any non-changing,
 143 “universally” valid rules governing the composition and microstructure of biological
 144 tissues. Inspired by Rupert Riedl (1925–2005), the eminent Austro-American zool-
 145 ogist of the second half of the twentieth century, who stressed that “*the living world*
 146 *happens to be crowded by universal patterns of organizations, which, most obviously,*
 147 *find no direct explanation through environmental conditions or adaptive radiation*”

148 [127], we here report on the successful finding of mathematical rules reflecting the
149 aforementioned patterns. Therefore, we apply an engineering science approach to
150 the structural biology of bone tissue, also assessing how such rules or patterns affect
151 the mechanical properties of bone tissue. For this purpose, we take into account the
152 well-known fact that bone tissue features a distinctive hierarchical organization [46,
153 78, 150], as seen in Fig. 1 and described in greater detail in Sect. 2. The involved
154 organizational patterns (specific arrangements of water, hydroxyapatite-type mineral,
155 and organic matter) can be found throughout different anatomical locations,
156 different organs, and different species. However, the *dosages* of distinctive features
157 within a specific material microstructure may well differ. These dosages follow the
158 aforementioned “universal” composition rules, which arise from a vast amount of
159 experimental data available in literature.

160 In particular, dehydration-demineralization tests, dehydration-deorganization
161 tests, and dehydration-ashing tests were analyzed in order to quantify the relations
162 between the mass density of extracellular bone matrix and the apparent mass densities
163 of water, hydroxyapatite, and organic matter, see Sect. 3. Furthermore, mass
164 and volume measurements on wet, dehydrated, and demineralized bone tissue samples,
165 as well as optical densities obtained from transmission electron microscopy
166 (TEM) of similar tissues are employed for assessing the distribution of hydroxyapatite
167 within extracellular bone matrix, see Sect. 4. Thereafter, a swelling rule for
168 hydrating collagenous tissues derived from processing and comparing data collected
169 from X-ray diffraction, vacuum drying, and mass measurements, is presented
170 in Sect. 5. Based on a mass conversation law formulated for closed systems representing
171 both the bone ultrastructure, as well as the fibrillar and extrafibrillar spaces,
172 the bone tissue evolution during mineralization can be predicted, see Sect. 6. Finally,
173 we present how the hierarchical organization of bone tissue can be “translated” into
174 a corresponding multiscale homogenization scheme, which allows for prediction of
175 the macroscopic tissue stiffness. The corresponding microelastic model also incorporates
176 the aforementioned four composition rules, so that they eventually govern
177 “universal” structure-property relations in bone, as described in Sect. 7.

178 2 Morphological Patterns of Bone

179 Bone materials are characterized by an astonishing variability and diversity. Still, the
180 fundamental hierarchical organization, or “once-chosen” basic “construction plans”
181 of bone materials have remained largely unchanged during biological evolution; this
182 has been coined, by Gould and Lewontin [52], as an “architecturally constrained”
183 situation. The aforementioned construction plans are reflected by typical morphological
184 features (or patterns) which can be discerned across most bone organs and tissues
185 occurring in the vertebrate kingdom. The corresponding hierarchical organization of
186 bone can be described by means of the following five levels [78]:

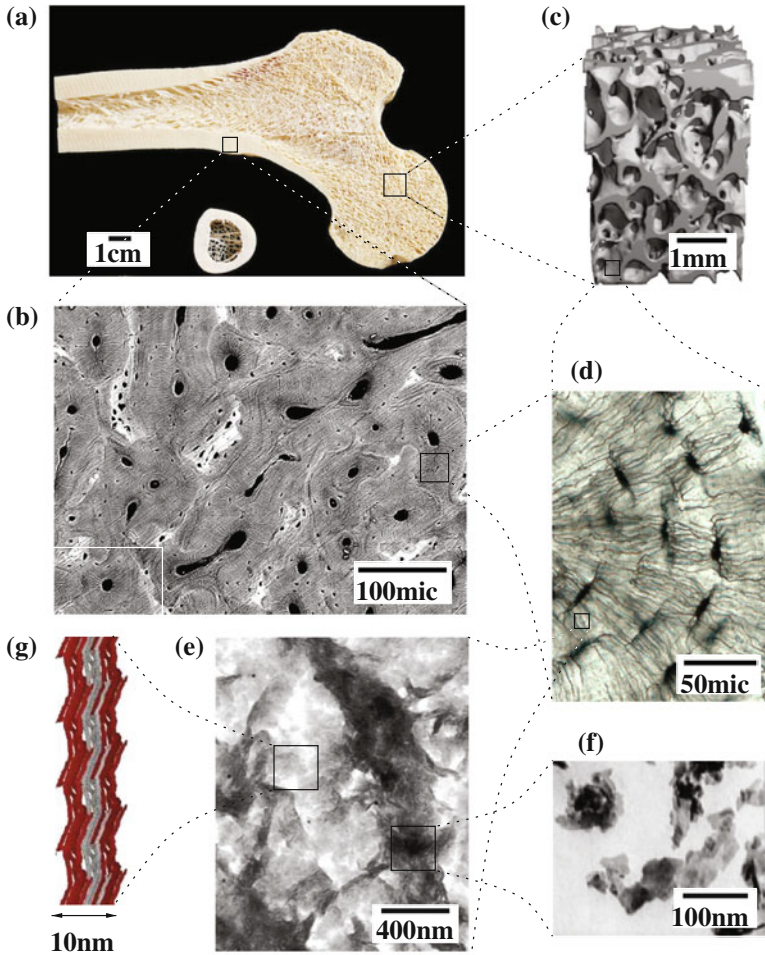


Fig. 1 Hierarchical organization of bone: **a** photograph of a cross-section through and across a whole long bone (copyright Ralph Hutchings/Visuals Unlimited, Inc.), showing the macrostructure; microstructure featuring either **b** osteonal cortical bone, acquired by SEM [58], or **c** trabecular struts making up trabecular bone, visualized based on micro-computed tomography data [103]; **d** osteocytic lacunae (brightfield light microscopy image taken by Tim Arnett); **e** ultrastructure, [122]; **f** hydroxyapatite crystals, obtained by means of SEM [150]; **g** wet collagen, electron density map of [112] (permission for reproduction requested from publisher: **b** The Royal Society; **c** ASME; **d** Annual Reviews; **e** Springer; **g** PNAS)

- 187 ● The macrostructure, with a characteristic length of several millimeters to centimeters, features cortical (or compact) bone and trabecular (or spongy) bone, see Fig. 1a.
- 188
- 189
- 190 ● Zooming out pieces of cortical bone, see Fig. 1b, or trabecular bone, see Fig. 1c, reveals that actually both materials are porous in nature: The corresponding vascular porosity hosts various biological cells as well as blood vessels; in cortical bone this porosity is organized in a tree-type branching structure of canals (called Haversian canals if parallel to the main bone axis, and Volkmann canals at the branching junctions [24, 29]); and in trabecular bone, these canals are penetrating each other, yielding eventually a microstructure made up by single plates or struts [54]. The vascular pore channels are connected, via much smaller channels called canaliculi, to cave-like single pores called lacunae [138], populated by individual osteocytes, and seen as small black dots in Fig. 1d.
- 192
- 193
- 194
- 195
- 196
- 197
- 198
- 199
- 200 ● The entire domain outside the vascular, lacunar, and canalicular porosities is called extracellular space or matrix. It appears as a nanocomposite with a characteristic size of several micrometers, see Fig. 1e. Within this extracellular space, collagen-rich domains, see the light areas in Fig. 1e, and collagen-free domains, see the dark areas in Fig. 1e, can be distinguished, the characteristic length of both of which is several hundred nanometers. Commonly, these domains are referred to as fibrils and extrafibrillar space [122].
- 202
- 203
- 204
- 205
- 206
- 207 ● Finally, the so-called elementary components of mineralized tissues can be distinguished, with a characteristic lengths in the range of nanometers:
- 208
- 209 – plate-shaped mineral crystals consisting of impure hydroxyapatite (HA, $\text{Ca}_{10}[\text{PO}_4]_6[\text{OH}]_2$) with typical 1–5 nm thickness, and 25–50 nm length [150], see Fig. 1f;
- 210
- 211
- 212 – slender, helically round collagen molecules with a diameter of about 1.2 nm and a length of about 300 nm [21, 112, 120], which are self-assembled in staggered organizational schemes (fibrils) with characteristic diameters of 50–500 nm [35, 95, 105, 122, 125, 142, 150, 151], see Fig. 1g – several covalently bonded fibrils are sometimes referred to as fibers;
- 213
- 214
- 215
- 216
- 217 – different non-collagenous organic molecules, predominantly lipids and proteins [73, 146]; and
- 218
- 219 – water.

220 Both the amount of these components, as well as their distribution across the hierarchical levels described above, are the focus of the subsequent sections.

221

222 3 Mineral and Collagen Dosages in Extracellular Bone

223 Matrix

224 Data from bone drying, demineralization, and deorganification tests, collected over a time span of more than 80 years [13, 25, 51, 57, 87, 90–92, 96], evidence a myriad of different chemical compositions of different bone materials. However, careful

225

226

analysis of the data, as to extract the chemical concentrations of hydroxyapatite, water, and organic matter¹ in the extracellular bone matrix, reveals an astonishing fact [147]: it appears that there exists a unique bilinear relationship between organic concentration and mineral concentration, across different species, different organs, and different age groups, from early childhood to old age.

Corresponding experimental endeavors typically started with the determination of the “macroscopic” mass density, i.e. that associated to millimeter-sized bone samples, by means of Archimedes’ principle. Therefore, the mass of the (wet) bone sample is first measured in air, delivering the quantity M_{air}^{μ} . Thereafter, the weight of the bone sample when submerged in a liquid, is quantified as W_{sub}^{μ} . Both quantities then give access to the volume of the millimeter-sized sample, through

$$V^{\mu} = \frac{1}{\rho_{\text{liquid}}} \left(M_{\text{air}}^{\mu} - \frac{W_{\text{sub}}^{\mu}}{g} \right), \quad (1)$$

with ρ_{liquid} as the mass density of the employed liquid, and g as the gravitational acceleration, $g = 9.81 \text{ m/s}^2$. Finally, the macroscopic mass density of the investigated samples follows from

$$\rho^{\mu} = \frac{M_{\text{air}}^{\mu}}{V^{\mu}}. \quad (2)$$

After having determined the samples’ mass density, the experimenters typically turned towards determination of the samples’ chemical composition; by one of three different experimental modalities, as described next.

Dehydration-Demineralization Tests

In a series of seminal experimental campaigns [87, 90, 91, 96], see Tables 1, 2 and 3, numerous millimeter-sized bone samples were first dried in a vacuum desiccator at room temperature, until a constant mass was observed, namely the mass of the dehydrated bone sample, M_{dry}^{μ} . The difference between the mass of wet sample in air and the mass of dehydrated sample obviously equals the mass of water which was originally contained in the sample, $M_{\text{H}_2\text{O}}^{\mu} = M_{\text{air}}^{\mu} - M_{\text{dry}}^{\mu}$. This water had filled all the bone pore spaces, from the vascular pore space seen in Fig. 1b, c, via the lacunar and canalicular pore spaces seen in Fig. 1d, down to the inter-crystalline and intermolecular pore spaces, as seen in Fig. 1e, f, g. Next, the samples were rehydrated and then demineralized in a 0.5 M ethylenediaminetetraacetic acid (EDTA) solution at pH 7.5, until no calcium was detected anymore by an atomic absorption spectrometer. After drying such a demineralized sample in vacuum, one is left with the organic mass which had been contained in the originally mineralized and wet bone sample, M_{org}^{μ} . Finally, knowledge of the masses of organic matter and water gives access to the hydroxyapatite mass, $M_{\text{HA}}^{\mu} = M_{\text{air}}^{\mu} - M_{\text{org}}^{\mu} - M_{\text{H}_2\text{O}}^{\mu}$. Thereafter, the constituent masses can be readily converted into weight fractions, through

¹90% of which is collagen [146].

Table 1 Bone composition from dehydration-demineralization experiments of Lees et al. [91]^a and Lees et al. [96]^b

Tissue	ρ^{μ} (g/cm ³)	WF _{HA} ^{μ} (-)	WF _{org} ^{μ} (-)	WF _{H₂O} ^{μ} (-)
Bovine tibia ^a	2.06	0.658	0.219	0.123
Bovine tibia ^a	2.05	0.656	0.219	0.126
Bovine tibia ^a	2.02	0.621	0.239	0.140
Bovine tibia ^a	2.02	0.627	0.232	0.140
Bovine tibia ^a	2.00	0.643	0.227	0.129
Bovine tibia ^a	2.05	0.643	0.230	0.127
Bovine tibia ^a	2.10	0.671	0.211	0.118
Bovine tibia ^a	2.08	0.664	0.216	0.120
Bovine tibia ^a	2.12	0.661	0.215	0.123
Bovine tibia ^a	2.08	0.663	0.221	0.116
Bovine tibia ^a	2.10	0.647	0.224	0.129
Bovine tibia ^a	1.98	0.654	0.217	0.128
Bovine tibia ^a	2.05	0.644	0.227	0.129
Bovine tibia ^a	2.11	0.649	0.229	0.122
Bovine tibia ^a	2.03	0.638	0.213	0.123
Bovine tibia ^a	2.06	0.699	0.184	0.117
Bovine tibia ^a	2.02	0.658	0.219	0.123
Bovine tibia ^a	1.99	0.656	0.219	0.126
Bovine tibia ^a	1.95	0.640	0.228	0.131
Bovine tibia ^a	2.01	0.659	0.218	0.123
Bovine tibia ^a	2.04	0.638	0.242	0.121
Bovine tibia ^a	2.05	0.674	0.210	0.116
Whale malleus ^b	2.49	0.860	0.100	0.040
Whale malleus ^b	2.45	0.800	0.130	0.070
Whale incus ^b	2.50	0.860	0.090	0.050
Whale stapes ^b	2.42	0.810	0.130	0.060
Whale stapes ^b	2.36	0.800	0.140	0.060
Whale periotic ^b	2.40	0.810	0.130	0.070
Whale periotic ^b	2.48	0.830	0.110	0.060
Whale periotic ^b	2.52	0.850	0.100	0.050
Whale periotic ^b	2.52	0.850	0.100	0.050
Whale periotic ^b	2.58	0.870	0.090	0.040
Whale t. bulla ^b	2.48	0.850	0.100	0.050

Table 2 Mineralized tendon composition from dehydration-demineralization experiments of Lees and Page [90]

Tissue	ρ^μ (g/cm ³)	WF _{HA} ^{μ} (-)	WF _{org} ^{μ} (-)	WF _{H₂O} ^{μ} (-)
Mineralized turkey leg tendon	1.33	0.286	0.250	0.465
Mineralized turkey leg tendon	1.50	0.445	0.239	0.316
Mineralized turkey leg tendon	1.50	0.410	0.217	0.374
Mineralized turkey leg tendon	1.51	0.437	0.217	0.346
Mineralized turkey leg tendon	1.52	0.454	0.239	0.308
Mineralized turkey leg tendon	1.52	0.437	0.219	0.343
Mineralized turkey leg tendon	1.52	0.396	0.244	0.360
Mineralized turkey leg tendon	1.53	0.443	0.222	0.335
Mineralized turkey leg tendon	1.54	0.459	0.244	0.297
Mineralized turkey leg tendon	1.58	0.473	0.228	0.299
Mineralized turkey leg tendon	1.58	0.462	0.217	0.321
Mineralized turkey leg tendon	1.59	0.476	0.228	0.297
Mineralized turkey leg tendon	1.60	0.487	0.230	0.283
Mineralized turkey leg tendon	1.61	0.459	0.230	0.310
Mineralized turkey leg tendon	1.61	0.495	0.244	0.261
Mineralized turkey leg tendon	1.62	0.500	0.228	0.272
Mineralized turkey leg tendon	1.64	0.506	0.228	0.266

$$WF_i^\mu = \frac{M_i^\mu}{M_{air}^\mu}, \quad i = \text{org, HA, H}_2\text{O}, \quad (3)$$

see Tables 1, 2 and 3. The weight fractions obviously fulfill

$$WF_{H_2O}^\mu + WF_{HA}^\mu + WF_{org}^\mu = 1. \quad (4)$$

Table 3 Bone composition from dehydration-demineralization experiments of Lees [87]

Tissue	$WF_{HA}^{\mu} (-)$	$WF_{org}^{\mu} (-)$	$WF_{H_2O}^{\mu} (-)$	$\rho^{\mu} (g/cm^3)$
Horse metacarpal	0.55	0.25	0.2	1.79
Horse metacarpal	0.57	0.26	0.17	1.84
Horse metacarpal	0.55	0.26	0.19	1.80
Horse metacarpal	0.54	0.28	0.18	1.79
Horse metacarpal	0.62	0.26	0.12	1.96
Horse metacarpal	0.62	0.27	0.11	1.97
Horse metacarpal	0.62	0.26	0.12	1.96
Horse metacarpal	0.61	0.26	0.13	1.94
Horse metacarpal	0.62	0.25	0.13	1.95
Horse metacarpal	0.54	0.23	0.23	1.75
Horse metacarpal	0.53	0.24	0.23	1.74
Horse metacarpal	0.54	0.27	0.19	1.79
Horse metacarpal	0.63	0.22	0.15	1.94
Horse metacarpal	0.62	0.25	0.13	1.95
Horse metacarpal	0.62	0.26	0.12	1.96
Horse metacarpal	0.64	0.23	0.13	1.98
Horse metacarpal	0.62	0.26	0.12	1.96
Horse metacarpal	0.66	0.23	0.12	1.99
Horse metacarpal	0.63	0.24	0.13	1.96

266 *Dehydration-Deorganization Tests*

267 Gong et al. [51] weighed several (macroscopic) bone samples in the wet state, as
 268 well as after drying at 80°C for 72 h - thereby getting access to their wet and dry
 269 masses, M_{air}^{μ} and M_{dry}^{μ} . As before, their difference is equal to the mass of water in the
 270 investigated bone sample, $M_{H_2O}^{\mu} = M_{air}^{\mu} - M_{dry}^{\mu}$. Next, the samples were freed from
 271 fat and other organic material, using, in a soxhlet apparatus, a mixture of 80% ethyl
 272 ether and 20% ethanol, as well as an 80% aqueous solution of ethylene diamine.
 273 After drying such a deorganized sample at 80°C (until constant weight is attained),
 274 one is left with the hydroxyapatite mass contained in the investigated bone sample,
 275 M_{HA}^{μ} . Finally, when knowing the mass of hydroxyapatite and water contained in the
 276 originally wet bone sample, as well as its original mass, the mass of the organic matter
 277 can be readily determined through $M_{org}^{\mu} = M_{air}^{\mu} - M_{HA}^{\mu} - M_{H_2O}^{\mu}$, together with the
 278 corresponding weight fractions according to Eq. (3), see Table 4.

279 *Dehydration-Ashing Tests*

280 In an interesting experimental campaign of Biltz and Pellegrino [13], cortical bone
 281 samples were dried until a constant mass, i.e. the dry bone mass, M_{dry}^{μ} , was attained,
 282 which, together with the original mass of the sample in air, M_{air}^{μ} , gives access to the
 283 mass of water in the investigated bone sample, $M_{H_2O}^{\mu}$. Next, the dried bones were

Table 4 Bone composition from dehydration-deorganification experiments of Gong et al. [51]

Tissue	ρ^μ (g/cm ³)	WF _{HA} ^{μ} (-)	WF _{org} ^{μ} (-)	WF _{H₂O} ^{μ} (-)
Steer tibial shaft	2.00	0.630	0.244	0.126
Dog femoral shaft	2.00	0.630	0.259	0.111
Humar femur and tibia	1.99	0.642	0.239	0.119
Monkey femur	2.04	0.643	0.239	0.117
Steer atlas bone	1.93	0.588	0.266	0.146
Dog lumbar vertebrae	1.91	0.582	0.265	0.153
Human thoracic and lumbar vertebrae	1.92	0.601	0.258	0.140
Monkey lumbar vertebrae	1.88	0.582	0.274	0.144

gently incinerated until all organic matter was burned off. Subsequent weighing evidenced the ash weight, M_{ash}^μ . As also some inorganic matter, namely 6.6% of the ash weight, is burned at an ashing temperature of 600°C [51], the ash mass provides access to the mineral mass, according to $M_{\text{HA}}^\mu = 1.066 \times M_{\text{ash}}^\mu$. The mass of organic matter follows from $M_{\text{org}}^\mu = M_{\text{air}}^\mu - M_{\text{HA}}^\mu - M_{\text{H}_2\text{O}}^\mu$. The corresponding weight fractions can be determined through Eqs. (3) and (4), which, in turn, provide access to ρ^μ , through

$$\rho^\mu = \left(\frac{\text{WF}_{\text{org}}^\mu}{\rho_{\text{org}}} + \frac{\text{WF}_{\text{HA}}^\mu}{\rho_{\text{HA}}} + \frac{\text{WF}_{\text{H}_2\text{O}}^\mu}{\rho_{\text{H}_2\text{O}}} \right)^{-1}, \quad (5)$$

where $\rho_{\text{org}} = 1.42 \text{ g/cm}^3$, $\rho_{\text{HA}} = 3 \text{ g/cm}^3$, and $\rho_{\text{H}_2\text{O}} = 1 \text{ g/cm}^3$ are the constituents' real mass densities [51, 60, 86]. For a compilation of data derived from [13], see Table 5. For the sake of completeness, it should be noted that [13] actually reported the volume fraction of water

$$f_{\text{H}_2\text{O}}^\mu = \frac{M_{\text{air}}^\mu - M_{\text{dry}}^\mu}{V^\mu}, \quad (6)$$

and the weight fraction of ash per mass of dried bone

$$\text{WF}_{\text{ash}}^{\text{dry}} = \frac{M_{\text{ash}}^\mu}{M_{\text{air}}^\mu - M_{\text{H}_2\text{O}}^\mu}. \quad (7)$$

Similar test campaigns were performed by [25, 57], see Table 6 for a compilation of test results.

Table 5 Bone composition from dehydration-ashing experiments of Biltz and Pellegrino [13]

Femoral and tibial samples of	ρ^μ (g/cm ³)	WF _{HA} ^{μ} (-)	WF _{org} ^{μ} (-)	WF _{H₂O} ^{μ} (-)
Fish	1.80	0.507	0.273	0.220
Turtle	1.81	0.529	0.266	0.204
Frog	1.93	0.572	0.246	0.182
Polar bear	1.92	0.583	0.245	0.172
Man	1.94	0.657	0.263	0.080
Elephant	2.00	0.658	0.242	0.100
Monkey	2.09	0.653	0.237	0.110
Cat	2.05	0.652	0.233	0.115
Horse	2.02	0.648	0.228	0.124
Chicken	2.04	0.653	0.227	0.120
Dog	1.94	0.637	0.219	0.144
Goose	2.04	0.669	0.218	0.113
Cow	2.05	0.660	0.212	0.128
Guinea Pig	2.10	0.669	0.212	0.119
Rabbit	2.12	0.685	0.199	0.116
Rat	2.24	0.713	0.197	0.090

301 *Determination of Tissue-Specific Volume Fractions*

302 Determination of the extracellular volume fractions of mineral and collagen, f_{HA}^{excel}
 303 and f_{col}^{excel} , rests on the aforementioned volume and weighing measurements on wet,
 304 dehydrated, and demineralized bone specimens, and on techniques revealing the bone
 305 microstructure, such as light microscopy, confocal microscopy, or micro-computed
 306 tomography. These imaging techniques give access to the so-called microporosity
 307 $f_{\mu por}$, the sum of the vascular, lacunar, and canalicular porosities,

$$308 \quad f_{\mu por} = f_{vas} + f_{lac} + f_{can} . \quad (8)$$

309 Vascular porosity in cortical bone, also called Haversian porosity in that context,
 310 ranges from 2% to typically 8% [19, 20, 30, 36, 140]. Under severe conditions such
 311 as bone disease like osteoporosis, overtraining, or drug treatment, it may increase
 312 up to 20% [140]. In trabecular bone, the vascular porosity ranges from 30 to 90%
 313 [27]. On the other hand, the much smaller lacunar and canalicular porosities lie within
 314 a much narrower range of values; in recent years, they were quantified by micro-
 315 computed tomography. In this context, [137, 138] reported 1.3 and 0.7% lacunar and
 316 canalicular porosity values, respectively. These values are close to those reported by
 317 Palacio-Mancheno [113], Tommasini et al. [144], and Hesse et al. [70]. Considering
 318 3% vascular porosity as relevant for mammalian bone of medium-to-large-sized
 319 animals (see e.g. evaluation of microscopic images of Lees et al. [91] as reported in

Table 6 Bone composition from dehydration-ashing experiments of Burns [25]^a and Hammett [57]^b

Tissue	WF _{HA} ^μ (-)	WF _{org} ^μ (-)	WF _{H₂O} ^μ (-)	ρ ^μ (g/cm ³)
Rabbit limb bones ^a	0.267	0.202	0.392	1.38
Rabbit limb bones ^a	0.210	0.194	0.581	1.25
Rat leg bones ^a	0.389	0.231	0.313	1.54
Rat leg bones ^a	0.345	0.224	0.375	1.46
Rat leg bones ^a	0.398	0.232	0.318	1.54
Rat leg bones ^a	0.378	0.218	0.334	1.52
Rat leg bones ^a	0.376	0.230	0.344	1.51
Humerus of rat ^b	0.171	0.180	0.650	1.20
Humerus of rat ^b	0.176	0.191	0.633	1.21
Humerus of rat ^b	0.235	0.199	0.567	1.27
Humerus of rat ^b	0.315	0.210	0.475	1.37
Humerus of rat ^b	0.337	0.208	0.456	1.40
Humerus of rat ^b	0.378	0.215	0.407	1.46
Humerus of rat ^b	0.434	0.222	0.344	1.55
Humerus of rat ^b	0.175	0.194	0.631	1.21
Humerus of rat ^b	0.180	0.193	0.627	1.21
Humerus of rat ^b	0.264	0.205	0.532	1.31
Humerus of rat ^b	0.315	0.209	0.476	1.37
Humerus of rat ^b	0.362	0.209	0.429	1.44
Humerus of rat ^b	0.420	0.219	0.361	1.53
Humerus of rat ^b	0.451	0.229	0.320	1.58
Femur of rat ^b	0.133	0.182	0.685	1.17
Femur of rat ^b	0.144	0.191	0.665	1.18
Femur of rat ^b	0.201	0.204	0.595	1.24
Femur of rat ^b	0.283	0.217	0.500	1.34
Femur of rat ^b	0.315	0.210	0.475	1.37
Femur of rat ^b	0.356	0.217	0.427	1.43
Femur of rat ^b	0.413	0.230	0.357	1.52
Femur of rat ^b	0.143	0.197	0.660	1.18
Femur of rat ^b	0.150	0.195	0.655	1.19
Femur of rat ^b	0.235	0.208	0.557	1.28
Femur of rat ^b	0.288	0.213	0.499	1.34
Femur of rat ^b	0.338	0.214	0.448	1.41
Femur of rat ^b	0.401	0.222	0.377	1.50
Femur of rat ^b	0.430	0.235	0.336	1.55

320 Fritsch and Hellmich [46]), we account for 5% microporosity $f_{\mu\text{por}}$ when assessing
 321 the extracellular (ultrastructural) characteristics of the bones tested by Biltz and
 322 Pellegrino [13], Burns [25], Gong et al. [51], Hammet [57], Lees [87], Lees et al.
 323 [91]. Accordingly, the extracellular mass density reads as

$$324 \quad \rho^{\text{excel}} = \frac{\rho^{\mu} - \rho_{\text{H}_2\text{O}} \times f_{\mu\text{por}}}{1 - f_{\mu\text{por}}}, \quad (9)$$

325 and the weight fraction of water-filled micropores (i.e. vascular, lacunar, and canalic-
 326 ular pores) in (wet) bone specimens reads as

$$327 \quad \text{WF}_{\mu\text{por}}^{\mu} = \frac{\rho_{\text{H}_2\text{O}} \times f_{\mu\text{por}}}{\rho^{\mu}}. \quad (10)$$

328 $\text{WF}_{\mu\text{por}}^{\mu}$ allows for scale transition from the macroscopic (microstructural) to the
 329 extracellular (ultrastructural) scale,

$$330 \quad \text{WF}_{\text{HA}}^{\text{excel}} = \frac{\text{WF}_{\text{HA}}^{\mu}}{1 - \text{WF}_{\mu\text{por}}^{\mu}}, \quad (11)$$

$$332 \quad \text{WF}_{\text{org}}^{\text{excel}} = \frac{\text{WF}_{\text{org}}^{\mu}}{1 - \text{WF}_{\mu\text{por}}^{\mu}}, \quad (12)$$

$$334 \quad \text{WF}_{\text{H}_2\text{O}}^{\text{excel}} = 1 - \text{WF}_{\text{HA}}^{\text{excel}} - \text{WF}_{\text{org}}^{\text{excel}}. \quad (13)$$

335 From Eqs. (5), (11)–(13), one can determine the apparent mass densities of organics,
 336 water, and hydroxyapatite through

$$337 \quad \rho_i^{\text{excel}} = \text{WF}_i^{\text{excel}} \rho^{\text{excel}}, \quad i = \text{org, HA, H}_2\text{O}. \quad (14)$$

338 The microporosity is negligible in size as regards the mineralized turkey leg tendon
 339 [34] and otic bones [159]. Thus, weight fractions and mass densities are not to be
 340 differentiated between the microstructural and the ultrastructural scale, as concerns
 341 the tissue samples of Lees and Page [90] and Lees et al. [96].

342 “Universal” Rules in Bone Fibrillogenesis and Mineralization

343 Applying the presented evaluation procedures to the collected experimental data, see
 344 Tables 1, 2, 3, 4, 5 and 6, results in a remarkable finding concerning the apparent
 345 mass densities of hydroxyapatite mineral, organic, and water; i.e. the masses of these
 346 constituents found in a millimeter-sized sample divided by the volume of the extra-
 347 cellular portion within this millimeter-sized sample; across a great variety of species,
 348 organs, and ages. The aforementioned apparent mass densities (or concentrations)
 349 strongly correlate with each other, see Fig. 2, as well as with the bone tissue mass
 350 density, see Fig. 3. Interestingly, all these correlations can be represented by bilinear
 351 functions, whereby the increasing branch depicted in Fig. 2a relates to tissues taken

352 from growing organisms (being in the states of childhood and adolescence), while
 353 the descending branch relates to tissues taken from adult organisms. The apparent
 354 mass densities can be translated into volume fractions through

$$355 \quad f_i^{\text{excel}} = \frac{\rho_i^{\text{excel}}}{\rho_i}, \quad i = \text{org, HA, H}_2\text{O}. \quad (15)$$

356 so that the constituents' volume fractions can be expressed by the following regres-
 357 sion functions depending on the extracellular mass density,

$$358 \quad \text{if } \rho^{\text{excel}} \leq 1.978 \text{ g/cm}^3 \quad \begin{cases} f_{\text{HA}}^{\text{excel}} = \frac{1}{\rho_{\text{HA}}} (1.3275\rho^{\text{excel}} - 1.3938), \\ f_{\text{org}}^{\text{excel}} = \frac{1}{\rho_{\text{org}}} (0.3888\rho^{\text{excel}} - 0.2393), \\ f_{\text{H}_2\text{O}}^{\text{excel}} = 1 - f_{\text{HA}}^{\text{excel}} - f_{\text{org}}^{\text{excel}}, \end{cases} \quad (16)$$

359 relating to growing organisms, and

$$360 \quad \text{if } \rho^{\text{excel}} \geq 1.978 \text{ g/cm}^3 \quad \begin{cases} f_{\text{HA}}^{\text{excel}} = \frac{1}{\rho_{\text{HA}}} (1.7298\rho^{\text{excel}} - 2.1895), \\ f_{\text{org}}^{\text{excel}} = \frac{1}{\rho_{\text{org}}} (-0.5180\rho^{\text{excel}} + 1.5541), \\ f_{\text{H}_2\text{O}}^{\text{excel}} = 1 - f_{\text{HA}}^{\text{excel}} - f_{\text{org}}^{\text{excel}}, \end{cases} \quad (17)$$

361 relating to aging organisms. As 90% of the organic matter in bone is collagen [146],
 362 the extracellular volume fraction of collagen follows as

$$363 \quad f_{\text{col}}^{\text{excel}} = 0.9 \times f_{\text{org}}^{\text{excel}}. \quad (18)$$

364 *Cell Biology Aspects*

365 It is interesting to discuss the mineral-versus-organics concentration relation of
 366 Fig. 2a from the viewpoint of cell biology: during growth, the mineral-to-organic
 367 mass apposition ratio in extracellular bone tissue is a constant, $d\rho_{\text{HA}}^{\text{excel}}/d\rho_{\text{org}}^{\text{excel}} = 3.4$,
 368 universally valid throughout different tissues of different growing species at different
 369 ages. This constant reflects the working mode of osteoblasts (cuboidal or polygonal
 370 bone cells with several tens of micrometers characteristic length [1, 17, 74, 111, 115,
 371 129, 158]. Pre-osteoblasts [41, 97, 115] deposit new osteoid, in the form of seams of
 372 some 8 to 10 μm thickness, made of proteoglycan gel reinforced by fairly randomly
 373 oriented collagen fibrils [26, 41, 155], see Fig. 4a. Thereafter, osteoblasts order the
 374 collagen fibrils through stretching [41], and mediate, through budding of matrix
 375 vesicles from cell processes [3], the precipitation of hydroxyapatite, see Fig. 4b. This
 376 results in the so-called primary mineralization [115], with a characteristic time of
 377 hours to days [152]. From a chemical viewpoint, specially synthesized matrix mole-
 378 cules, such as bone sialoprotein, osteopontin, or osteocalcin [153], induce mineral
 379 formation, and such non-collagenous organic molecules typically make up 10% of
 380 the overall organic volume fraction [24, 86, 146], regardless of the magnitude of
 381 the latter. Accordingly, one would expect the more mineral precipitation, the more

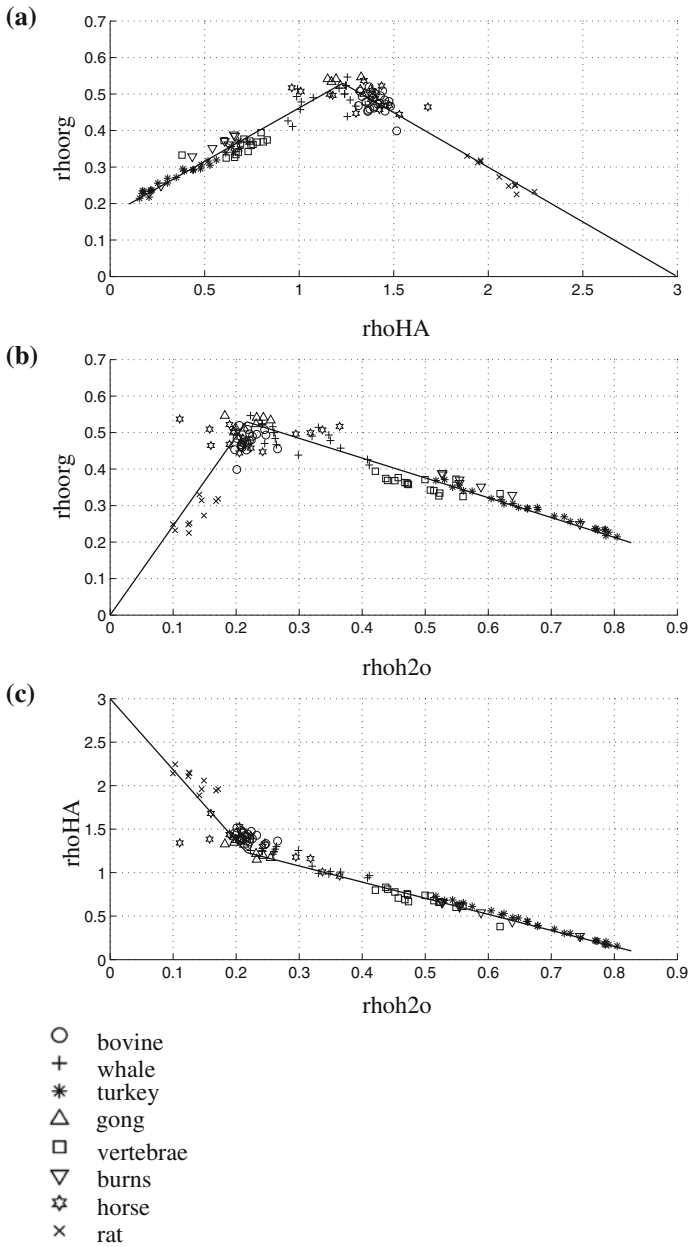


Fig. 2 Relations between apparent mass densities in extracellular bone matrix in the line of Vuong and Hellmich [147]: **a** hydroxyapatite versus organic matter, **b** water versus organic matter, and **c** water versus hydroxyapatite; across different species, organs, and ages

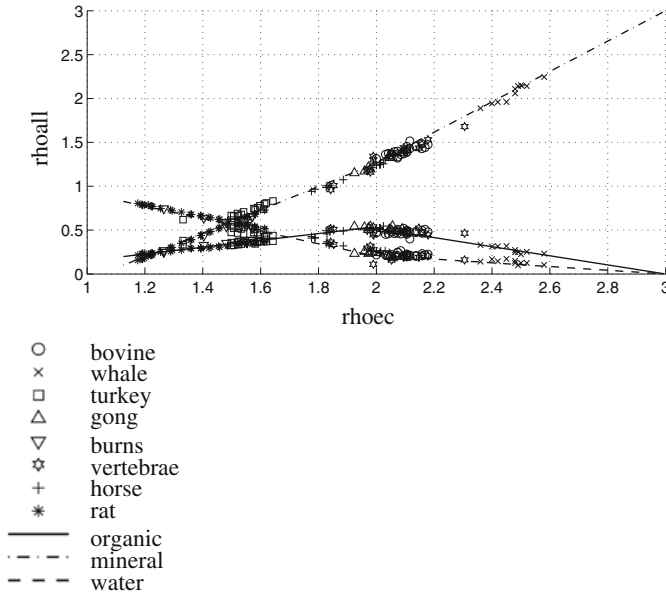


Fig. 3 Apparent mass densities of water, hydroxyapatite, and organic matter, versus overall mass density of extracellular bone matrix, ρ^{ecel} , across different species, organs, and ages

382 non-collagenous organics present, the amount of the latter being proportional to that
 383 of the overall organic matter. This is perfectly consistent with the aforementioned
 384 tissue- and species-independent, “universal” mineral-per-organics apposition ratio of
 385 3.4, suggesting primary mineralization as the dominant mineralization mechanism
 386 in growing organisms.

387 In such organisms, the mineral is hindered from further precipitation in the highly
 388 ionic fluids, through the action of the most abundant biological bone cells, namely
 389 the osteocytes [1, 10, 11, 18, 111, 115, 143], residing in the lacunar porosity of
 390 extravascular bone matrix. Originating from osteoblasts which were buried in the
 391 course of ongoing osteoid formation and mineralization, osteocytes maintain a widely
 392 spread network, through channels called canaliculi, among themselves and with the
 393 osteoblasts located at the bone tissue surface. This network is thought to effectively
 394 transfer mechanical stimuli related to tissue deformation, to the osteoblasts [17, 32],
 395 so as to trigger their bone formation activity, as described before. In addition to
 396 mechanosensing, osteocytes may inhibit mineralization around their lacunae [18],
 397 and therefore set an upper limit to the asymptotic mineral concentration which may
 398 be attained during the process called secondary mineralization. This process exhibits
 399 a characteristic time of weeks to months [9], see Fig. 4c, and before reaching its
 400 asymptote, secondary mineralization is not controlled by the local biological cells, but
 401 by the diffusion and composition properties of the fluids saturating the extracellular
 402 bone tissue [115]. However, at higher ages, the aforementioned inhibitive activity
 403 of osteocytes steadily decreases, so that, in the end, even the lacunae themselves

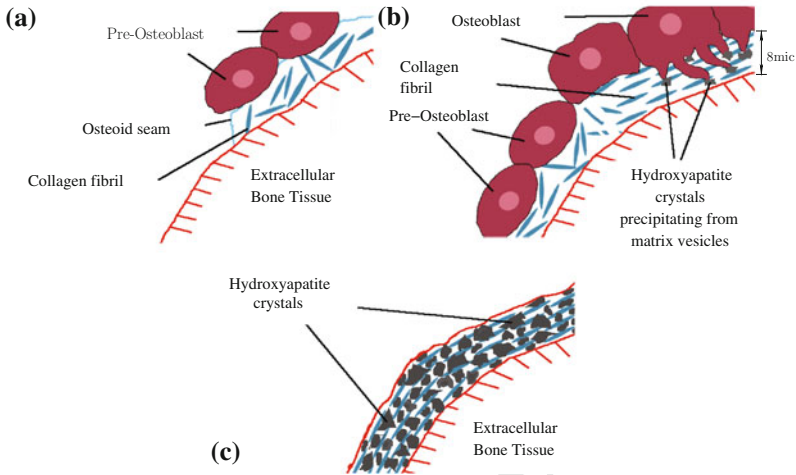


Fig. 4 Working mode of pre-osteoblasts and osteoblasts: primary and secondary mineralization of an unmineralized osteoid; **a** pre-osteoblasts lay down an osteoid seam, reinforced by randomly oriented collagen fibrils; **b** primary mineralization: osteoblasts order the collagen fibrils through cell-driven stretch, and mediate, through budding of matrix vesicles from cell processes, the precipitation of hydroxyapatite; **c** secondary mineralization: crystals grow without control of local biological cells

404 may be filled with mineral, as evidenced by [11, 49, 75]. As a consequence, the
 405 organic-to-mineral concentration ratio decreases and the mineral-to-organic mass
 406 apposition ratio is not equal to 3.4 anymore. At the same time, osteoblastic activity
 407 also decreases at more advanced ages [1], leading to a reduction of the (absolute)
 408 organic concentration in extracellular bone matrix. This combined effect of both
 409 osteoblastic and osteocytic activity reduction is expressed by a (negative) mineral-
 410 growth-to-organic-removal ratio, see Fig. 2a, which reveals secondary mineralization
 411 as the dominant mineralization mechanism in adult, aging organisms.

412 We also remark that the results presented here refer to physiologically normal
 413 conditions, while drug treatments may lead to considerable deviations from these
 414 rules for fibrillogenesis and mineralization, see [147] for further details.

415 4 Mineral Distribution in Extracellular Bone Matrix

416 At the ultrastructural observation scale (1–10 μm) of fully mineralized tissues, trans-
 417 mission electron micrographs (TEM) reveal that hydroxyapatite is situated both
 418 within and outside of the collagen fibrils, and that the majority of hydroxyapatite
 419 lies outside the fibrils [2, 101, 121, 122, 139, 159]. The question arises whether the
 420 distribution of mineral between the fibrillar and extrafibrillar spaces follows a general
 421 rule. And indeed, Hellmich and Ulm [63] found out that the average mineral con-

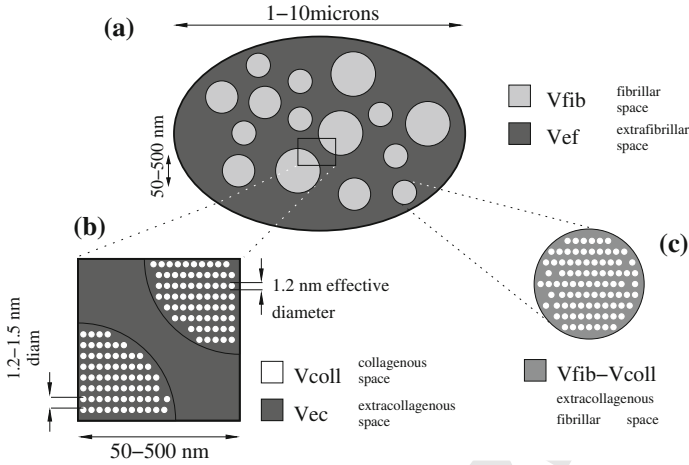


Fig. 5 Schematic sketch of spaces in the extracellular bone matrix or ultrastructure, **a** section through the ultrastructural representative volume element perpendicular to the direction of the fibrils, **b** and **c** close-ups

422 centration in the extrafibrillar space equals that in the extracollagenous space. The
 423 underlined arguments are as follows: The ultrastructural volume element with a char-
 424 acteristic size of some micrometers, consists of fibrillar and extrafibrillar space; see
 425 Fig. 5a, with corresponding volumes $V_{\text{fib}}^{\text{excel}}$ and $V_{\text{exfib}}^{\text{excel}}$. The fibrils are made up by col-
 426 lagen molecules exhibiting a triple helix structure arranged more or less cylindrically,
 427 with diameters ranging from 50 to 500 nm [35, 95, 105, 122, 125, 142, 150, 151].
 428 The fibrillar volume $V_{\text{fib}}^{\text{excel}}$ comprises all fibrils within the ultrastructural (or extra-
 429 cellular) volume $V_{\text{exfib}}^{\text{excel}}$. $V_{\text{col}}^{\text{fib}}$, the volume of collagen within the fibrils, is a subspace
 430 of $V_{\text{fib}}^{\text{excel}}$, as is $(V_{\text{fib}}^{\text{excel}} - V_{\text{col}}^{\text{fib}})$. The latter is the volume within the fibrils which is not
 431 occupied by collagen molecules, subsequently referred to as extracollagenous fibril-
 432 lar volume, $V_{\text{excol}}^{\text{fib}}$. The space within the ultrastructure (or extracellular bone matrix)
 433 that is not occupied by fibrils is called extrafibrillar space, $V_{\text{exfib}}^{\text{excel}} = V_{\text{excol}}^{\text{excel}} - V_{\text{col}}^{\text{fib}}$.
 434 The union of the spaces $V_{\text{exfib}}^{\text{excel}}$ and $V_{\text{excol}}^{\text{fib}}$, $V_{\text{exfib}}^{\text{excel}} + V_{\text{excol}}^{\text{fib}} = V_{\text{excol}}^{\text{excel}} - V_{\text{col}}^{\text{fib}}$,
 435 is the total extracollagenous space within the extracellular bone.

436 Based on these notions, the aforementioned rule would imply that the ratio of
 437 the mass of the extrafibrillarly located mineral ($M_{\text{HA}}^{\text{exfib}}$), over the volume of the
 438 extrafibrillar space needs to be equal to the ratio of the entire mineral mass (M_{HA}),
 439 over the extracollagenous volume

$$440 \quad \rho_{\text{HA}}^{\text{exfib}} = \frac{M_{\text{HA}}^{\text{exfib}}}{V_{\text{exfib}}^{\text{excel}}} \equiv \frac{M_{\text{HA}}}{V_{\text{excol}}^{\text{excel}}} = \rho_{\text{HA}}^{\text{excol}}, \quad (19)$$

441 with $\rho_{\text{HA}}^{\text{exfib}}$ and $\rho_{\text{HA}}^{\text{excol}}$ being the apparent mineral densities relating to the extrafibrillar
 442 and the extracollagenous volumes, respectively. Equation (19) can be rearranged as
 443 follows

$$\phi_{\text{HA}}^{\text{exfib}} = \frac{M_{\text{HA}}^{\text{exfib}}}{M_{\text{HA}}} \equiv \frac{V_{\text{exfib}}^{\text{excol}}}{V_{\text{excol}}^{\text{excol}}} = \frac{f_{\text{exfib}}^{\text{excol}}}{1 - f_{\text{col}}^{\text{excol}}}, \quad (20)$$

where $f_{\text{exfib}}^{\text{excol}} = V_{\text{exfib}}^{\text{excol}} / V_{\text{excol}}^{\text{excol}}$ is the extrafibrillar volume fraction, $f_{\text{col}}^{\text{excol}} = V_{\text{col}}^{\text{excol}} / V_{\text{excol}}^{\text{excol}}$ is the collagen volume fraction, both quantified within the volume of extracellular bone, and $\phi_{\text{HA}}^{\text{exfib}}$ is the relative amount of extrafibrillar mineral.

Two independent sets of experimental observations covering a large range of tissue mass densities were considered for checking the relevance of Eq. (20), as discussed next.

Experimental Set I: Mass and Volume Measurements

First, $f_{\text{exfib}}^{\text{excol}} / (1 - f_{\text{col}}^{\text{excol}})$ is determined from weighing experiments and diffraction spacing measurements. In order to determine the apparent mass density of collagen, we adopt a value of $\rho_{\text{org}} = 1.42 \text{ g/cm}^3$ [76, 86], and consider the fact that collagen constitutes approximately 90% by weight of the organic matter in mineralized tissues [13, 86, 146, 150]. The mass of organic matter can be determined from weighing experiments on demineralized and dehydrated specimens [13, 86, 90, 91], harvested from different anatomical locations of different vertebrates at different ages, see Sect. 2, in particular Tables 1, 2, 3 and 5. On the other hand, the determination of the extrafibrillar volume fraction $f_{\text{exfib}}^{\text{excol}} = 1 - f_{\text{fib}}^{\text{excol}}$ requires quantification of the fibrillar space within the mineralized tissue. This can be achieved by application of a model for the organization of collagen: we use Lees' generalized packing model [16, 86], as the simplest model to quantify the average crosslink length between collagen molecules, see also [63].

Experimental Set II: Transmission Electron Microscopy

As a second, independent set of observations, we consider optical density measurements from TEMs, in order to determine $\phi_{\text{HA}}^{\text{exfib}}$. Figure 6 displays three TEMs of cross sections of mineralized tissues, covering a wide range of extracellular mass densities; from $\rho^{\text{excol}} = 1.5 \text{ g/cm}^3$ for mineralized turkey leg tendon, see Fig. 6a, to $\rho^{\text{excol}} = 2.6 \text{ g/cm}^3$ for the rostrum of whale, see Fig. 6c. These micrographs reflect the electron density of material phases. The higher the electron density, the darker the respective area of the TEM images. Since hydroxyapatite exhibits by far the largest electron density of all elementary components, the TEM images displayed in Fig. 6 highlight that hydroxyapatite is mainly located outside the fibrils. First, the relative optical density is determined using the protocol of Lees et al. [95]: the TEM images are scanned and then captured by a frame grabber [22]. The optical density is considered to be linearly proportional to the number of electrons transmitted through the particular area [95], the number of electrons to be linearly proportional to the local hydroxyapatite mass density in the fibrillar or extrafibrillar space. The average densities are then related to the apparent mineral densities, allowing for the determination of the extrafibrillar volume fraction of tissues, $f_{\text{exfib}}^{\text{excol}}$, shown in TEM images. $f_{\text{exfib}}^{\text{excol}}$ turns out to be 60% for the mineralized turkey leg tendon micrograph of Fig. 6a ($\rho^{\text{excol}} = 1.5 \text{ g/cm}^3$), 53% for the human tibia ($\rho^{\text{excol}} = 2.0 \text{ g/cm}^3$), see Fig. 6b, and 85% for the whale rostrum ($\rho^{\text{excol}} = 2.6 \text{ g/cm}^3$), see Fig. 6c.

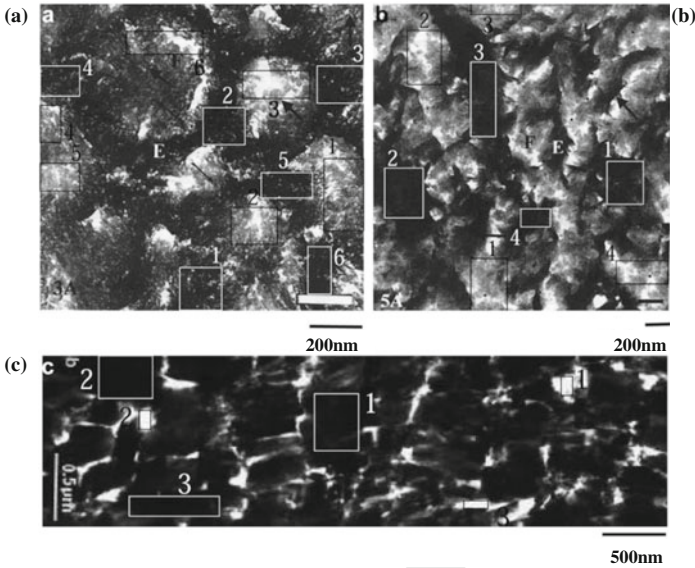


Fig. 6 Transmission electron micrographs of cross sections through: **a** mineralized turkey leg tendon [122]; **b** human tibia [122] and **c** whale rostrum [159]

485 **Comparison of Independently Derived Values of the Relative Amount of Extrafibrillar Mineral**
 486

487 Next, the sample-specific relative amount of extrafibrillar mineral, ϕ_{HA}^{exfib} , of very dif-
 488 ferent bone tissues, derived from the independent methods related to the experiment
 489 sets I and II, respectively, are compared, as shown in Fig. 7. It can be seen that the
 490 values derived from both experimental data sets are in perfect agreement when com-
 491 paring similar tissues. This surprisingly good agreement of values obtained from two
 492 independent assessment methods provides the sought after evidence that the aver-
 493 age mineral concentration in the extrafibrillar and the extracollagenous spaces are
 494 indeed equal; see Hellmich and Ulm [63] for further details.

495 **5 Hydration-Dependent Evolution of Unmineralized Collagenous Tissues**
 496

497 Hydration of collagenous tissues, consisting of fibrillar and extrafibrillar constituents,
 498 causes swelling, as well as mechanical softening (i.e. reduction of stiffness). The
 499 underlying mechanism can be quantified in terms of the following mathematical rule
 500 [109]: After drying the tissue in air, water remains only in the gap zones between
 501 the triple-helical collagen molecules making up 12% of the total volume [88]. Upon
 502 rehydration, the extrafibrillar space is established at volumes directly proportional to

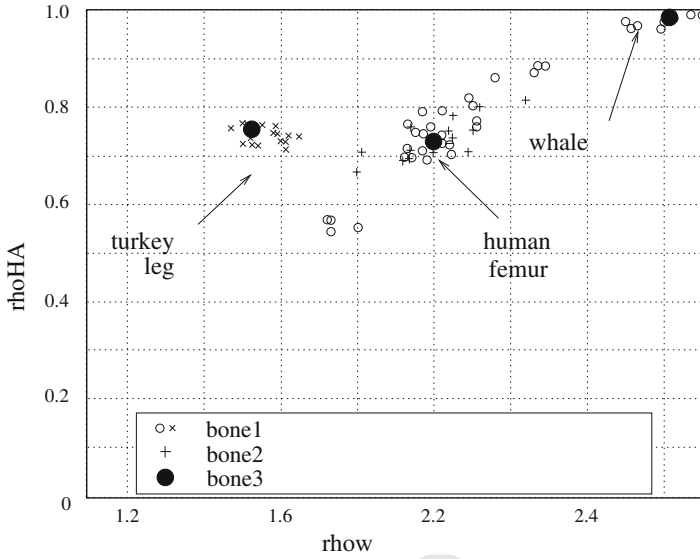


Fig. 7 Relative amount of extrafibrillar mineral, ϕ_{HA}^{exfib} , as a function of extracellular mass density ρ^{excel} , according to Hellmich and Ulm [63]

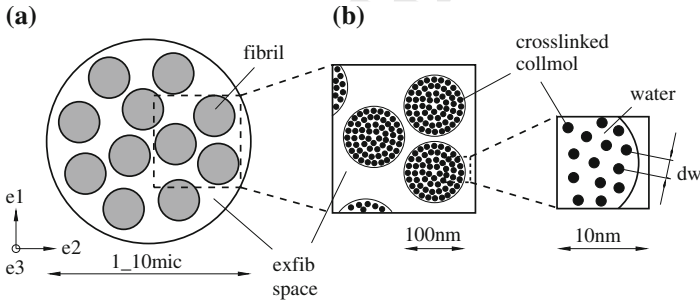


Fig. 8 Scheme concerning hierarchical structure of collagen: **a** collagenous tissue, **b** wet collagen

503 the hydration-induced swelling of the (micro) fibrils, until the maximum equatorial
 504 distance between the long collagen molecules is reached. Thereafter, the volume
 505 of the fibrils stays constant, and only the extrafibrillar volume continues to grow.
 506 Mathematically, the proportionality between the extrafibrillar space growth and the
 507 swelling of fibrils (given that the fibrils still swell, which occurs if they are not fully
 508 hydrated) can be expressed as follows

509
$$V_{exfib}^{excel} = \beta(V_{fib}^{excel} - V_{dry}^{col}), \quad V_{dry}^{col} \leq V_{fib}^{excel} \leq V_{fib,max}^{excel}, \quad (21)$$

with β as proportionality constant, with $V_{\text{exfib}}^{\text{excel}}$ as the volume of extrafibrillar space within the collagenous tissue, $V_{\text{fib}}^{\text{excel}}$ as fibrillar volume within the collagenous tissue, which is smaller than or equal to the maximum attainable value $V_{\text{fib,max}}^{\text{excel}}$, and larger than a minimum value $V_{\text{dry}}^{\text{col}}$ corresponding to the dry volume of the collagenous tissue, V^{excel} . The fibrillar and extrafibrillar volumes, $V_{\text{fib}}^{\text{excel}}$ and $V_{\text{exfib}}^{\text{excel}}$, fill the entire tissue volume V^{excel} , $V_{\text{fib}}^{\text{excel}} + V_{\text{exfib}}^{\text{excel}} = V^{\text{excel}}$, yielding together with (21) a tissue swelling rule in the following form

$$\frac{V^{\text{excel}}}{V_{\text{dry}}^{\text{col}}} = \beta \left(\frac{V_{\text{fib}}^{\text{excel}}}{V_{\text{dry}}^{\text{col}}} - 1 \right) + \frac{V_{\text{fib}}^{\text{excel}}}{V_{\text{dry}}^{\text{col}}}, \quad V_{\text{dry}}^{\text{col}} \leq V_{\text{fib}}^{\text{excel}} \leq V_{\text{fib,max}}^{\text{excel}}. \quad (22)$$

We regard the fibrils as continua with one to several hundreds of nanometers characteristic size, these continua being built up by representative volume elements of several to several tens of nanometers characteristic size, see Fig. 8. Microscopic images [28] show that hydration affects volume changes in a fibril in a homogeneous fashion. Therefore, following the deformation laws of continuum mechanics [131], the current fibrillar volume $V_{\text{fib}}^{\text{excel}}$ is related to the initial volume $V_{\text{dry}}^{\text{col}}$ by the Jacobian J , which is standardly expressed by the product of the principal stretches λ_1 , λ_2 , and λ_3 of the volume elements, thus

$$\frac{V_{\text{fib}}^{\text{excel}}}{V_{\text{dry}}^{\text{col}}} = J = \lambda_1 \cdot \lambda_2 \cdot \lambda_3. \quad (23)$$

The principal stretches are defined as the ratio of the current length to the initial length of the line elements $d\mathbf{x}_1$, $d\mathbf{x}_2$, and $d\mathbf{x}_3$ attached in the principal deformation directions to the elementary volume elements (see Fig. 8 for the orientations of principal line elements attached to the fibrils) and are related to the ratios of diffraction spacings in the current and initial elementary volumes, in the line of standard stretch measurements in lattice-like microstructures [148, 149]. As regards λ_1 and λ_2 , these diffraction spacings are related to the (on-average) lateral (transversal, equatorial) distances between collagen molecules,

$$\lambda_1 = \lambda_2 = \lambda_{\text{tr}} = \frac{d_w}{d_{\text{dry}}}, \quad (24)$$

with d_w as the lateral diffraction spacing related to some more or less hydrated state of the fibril, and $d_{\text{dry}} = 1.09 \text{ nm}$ as the lateral diffraction spacing in dry tissues [93]. As regards λ_3 , diffraction peaks relate to the axial macroperiod D_w of collagen, comprising repeating units of one gap zone and one overlap zone each, as discovered by Hodge and Petruska [72]; this axial macroperiod increases, albeit only slightly, upon hydration (up to a value of 67 nm). Since this increase is clearly less than 5% when compared to the axial macroperiod, $D_{\text{dry}} = 64 \text{ nm}$, measured in dry tissues, we consider D_w as a constant, and hence

$$\lambda_3 = \lambda_{ax} = \frac{D_w}{D_{dry}} = 1. \quad (25)$$

Finally, the variation of the current fibrillar volume with respect to the initial one reads as

$$\frac{V_{fib}^{excel}}{V_{dry}^{col}} = \lambda_1 \cdot \lambda_2 \cdot \lambda_3 = \left(\frac{d_w}{d_{dry}} \right)^2. \quad (26)$$

However, the diffraction spacings are limited, and cannot exceed a maximum value of 1.38 nm in the equatorial direction [102]. Therefore, the amount of water which can be accommodated in the fibrils is also limited. Upon further hydration, namely beyond the so-called fibrillar saturation limit, only the extrafibrillar volume continues to grow. The mathematically expressed swelling rule (21), together with volume relations (22) to (26), was experimentally validated by means of the measurement results of Meek et al. [102], Robinson [128], Rougvie and Bear [130]. Therefore, the water-to-organic ratios \mathcal{R} given in these papers, were converted into volumes according to

$$\frac{V^{excel}}{V_{dry}^{col}} = 0.88 \frac{\mathcal{R} \rho_{col} + \rho_{H_2O}}{\rho_{H_2O}}, \quad (27)$$

where $\rho_{col} = 1.42 \text{ g/cm}^3$ [88] and $\rho_{H_2O} = 1 \text{ g/cm}^3$ are the mass densities of molecular collagen and water, respectively; obviously, this equation accounts for the existence of 12% gap zones in the collagenous dry matrix [72, 88], relating to an intermolecular pore saturation limit amounting to $\mathcal{R}^{imsat} = 0.096$. Based on relations (22) and (27), combined with the observations of Meek et al. [102], that the fibrillar swelling stops at a water-to-organic mass ratio of $\mathcal{R}^{fibsatsat} = 0.82$, one can translate the swelling rule (22) into a mathematical relation between water-to-organic mass ratios and corresponding diffraction spacings,

$$\mathcal{R}^{pred} = \frac{1}{\rho_{col}} \left(\frac{\rho_{H_2O}}{0.88} \left[(\beta + 1) \left(\frac{d_w}{d_{dry}} \right)^2 - \beta \right] - \rho_{H_2O} \right). \quad (28)$$

It is directly tested against respective experimental values provided by Katz and Li [76], Meek et al. [102], Rougvie and Bear [130], see Fig. 9, with a relative error as low as $0.98 \pm 12.56\%$ (mean value plus standard deviation), see [109] for further details. Given the excellent confirmation of the swelling rule, it allows for quantifying the evolution of subvolumes and volume fractions in hydrating tissues: during hydration, the fibrillar volume fraction decreases by more than 50%, see Fig. 10b. At the same time, the tissue is swelling to its triple size, as seen in Fig. 10a. Also during hydration, the volume fraction of molecular collagen within a fibril decreases from 88 to 54.7%, while that of water increases from 0 to 45.3%, see Fig. 11b. At the same time, the fibrils grow by about 60% in volume, see Fig. 11a.

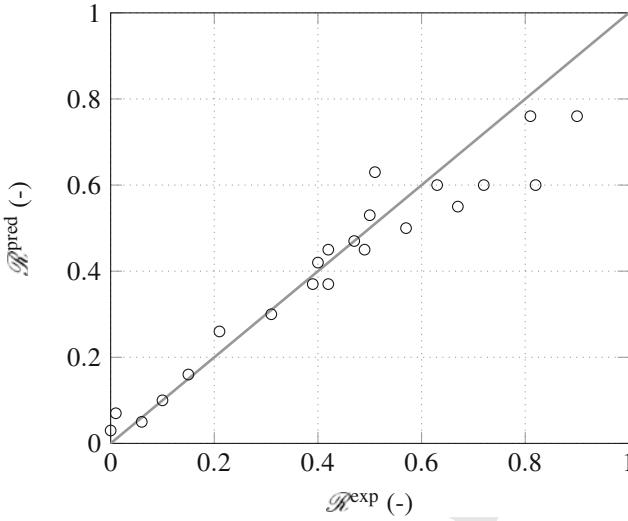


Fig. 9 Water-to-organic mass ratio: diffraction- and swelling rule-based predictions $\mathcal{R}^{\text{pred}}$ versus direct experiments \mathcal{R}^{exp}

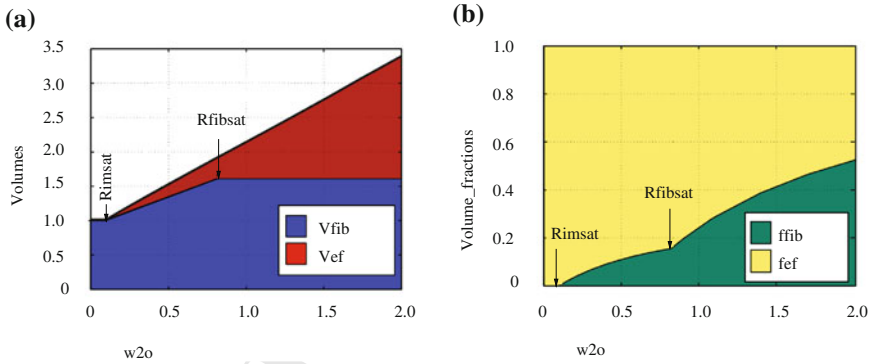


Fig. 10 Tissue swelling (a) and evolution of tissue composition (b) during hydration: **a** water-to-organic mass ratio \mathcal{R} over the fibrillar and extrafibrillar volumes making up the tissue; **b** water-to-organic mass ratio \mathcal{R} over the fibrillar and extrafibrillar volume fractions at the tissue scale

6 Bone Tissue Evolution During Mineralization

577

578 Inspired by an interesting idea of Lees [87], Morin and Hellmich [107] showed that
 579 the volume and structure changes in mineralizing bone tissues can be mathematically
 580 predicted when considering the extracellular bone tissue and its subvolumes (both
 581 the fibrils and the extrafibrillar space) as closed thermodynamic systems: i.e. if no
 582 fluid mass leaves or enters these volumes during the mineralization process, then
 583 the precipitation of hydroxyapatite crystals entails that the mass of lost ionic fluid

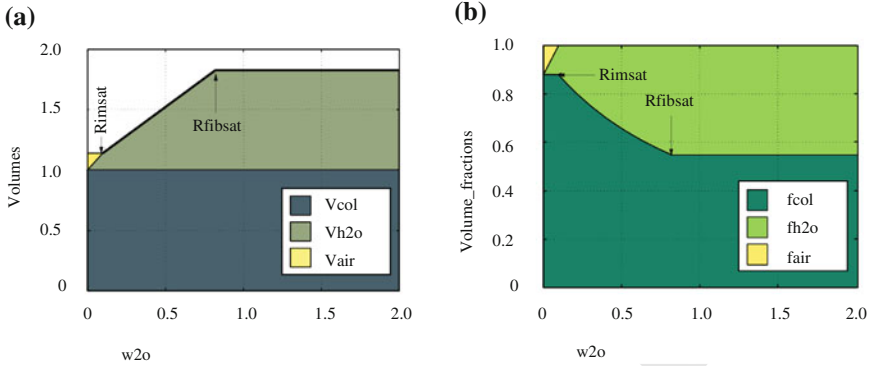


Fig. 11 Fibrillar swelling (a) and evolution of fibrillar composition (b) during hydration: **a** water-to-organic mass ratio R over the volumes of molecular collagen, water, and air making up the fibrils; **b** water-to-organic mass ratio R over the volume fractions of collagen, water, and air at the tissue scale

584 equals the mass of formed solid hydroxyapatite crystal in the fibrillar and extrafibrillar subvolumes, as well as in the entire tissue volume, while the collagen mass
 585 remains unaltered. The precipitation of dissolved ions into solid mineral crystals is
 586 accompanied by an increase in mass density, which, upon overall conservation under
 587 closed conditions, leads to a volume decrease (or shrinkage) of the tissues during the
 588 biomineralization process. This shrinkage affects both the fibrillar and the extrafibrillar
 589 tissue compartments. Thereby, the fibrillar shrinkage can be experimentally
 590 accessed through equatorial neutron diffraction spacings $d_{w,\infty}$, measured on fully
 591 mineralized tissues [104, 109]
 592

593

$$\left(\frac{d_{w,\infty}}{d_{w,0}}\right)^2 = \frac{V_{fib,\infty}^{excel}}{V_{fib,0}^{excel}}, \quad (29)$$

594 with $d_{w,0}$ as the neutron diffraction spacing at the time of osteoid deposition (i.e. the
 595 beginning of the mineralization process), and $V_{fib,0}^{excel}$ and $V_{fib,\infty}^{excel}$ as the fibrillar volume
 596 in unmineralized and fully mineralized tissues, respectively.

597 The mass density-diffraction relation (ρ_{∞}^{excel} - $d_{w,\infty}$ -relation) is derived in three
 598 consecutive steps: First, the mineralization-induced tissue shrinkage is evaluated at
 599 the tissue level, based on the “universal” composition rules described in Sect. 3,
 600 yielding [107]

601

$$\frac{V_{\infty}^{excel}}{V_0^{excel}} = \frac{1}{1 + (\rho_{HA}/\rho_{fl} - 1) \times f_{HA,\infty}^{excel}(\rho_{\infty}^{excel})}, \quad (30)$$

602 with V_0^{excel} and V_{∞}^{excel} as the extracellular tissue volumes at the beginning and the end
 603 of the mineralization process, ρ_{HA} and ρ_{fl} as the mass densities of hydroxyapatite

604 and ionic fluid, $f_{HA,\infty}^{excel}$ as the mineral volume fraction in the fully mineralized tissue,
 605 which depends on the tissue mass density, ρ_{∞}^{excel} .

606 Secondly, this relation is downscaled to the extrafibrillar space, by considering
 607 the equality of mineral concentrations in the extracollagenous and the extrafibrillar
 608 spaces [63], see Sect. 4, and the hydration swelling rule for unmineralized tissues
 609 [109], as described in Sect. 5. The corresponding volume change reads as [107]

$$610 \quad \frac{V_{exfib,\infty}^{excel}}{V_{exfib,0}^{excel}} = 1 + \frac{(1 - \rho_{HA}/\rho_{fl}) V_{\infty}^{excel}}{1 - f_{col,0}^{excel} V_0^{excel}} \times f_{HA,\infty}^{excel}(\rho_{\infty}^{excel}), \quad (31)$$

611 where $V_{\infty}^{excel}/V_0^{excel}$ obeys Eq. (30), $f_{HA,\infty}^{excel}(\rho_{\infty}^{excel})$ follows from the universal com-
 612 position rules (see Sect. 3), and $f_{col,0}^{excel}$ is the collagen volume fraction in unminer-
 613 alized tissue, which can be quantified from the hydration-dependent swelling rules
 614 described in Sect. 5, see [109] for details.

615 Thirdly, the fibrillar shrinkage is analogously derived,

$$616 \quad \frac{V_{fib,\infty}^{excel}}{V_{fib,0}^{excel}} = \frac{f_{fib,\infty}^{excel} V_{\infty}^{excel}}{f_{fib,0}^{excel} V_0^{excel}}, \quad (32)$$

617 where $f_{fib,\infty}^{excel} = 1 - f_{exfib,\infty}^{excel}$, and related to the change in diffraction spacing, as given
 618 in Eq. (29), with $d_{w,0} = d_{max} = 1.52$ nm as the diffraction spacing of fully saturated
 619 unmineralized collageneous tissues [23, 39, 76, 93]. Finally, these relations are
 620 translated into the sought mass density-diffraction spacing relations, according to
 621 continuum geometry and considering negligible length changes in the meridional
 622 direction of the tissue [109]. In case of fully-hydrated tissues, this relation reads as

$$623 \quad d_{w,\infty} = d_{max} \frac{1 - f_{exfib,0}^{excel} \times \left[1 - (\rho_{HA}/\rho_{fl} - 1) \times f_{HA,\infty}^{excel} \times \frac{f_{col,\infty}^{excel}}{\rho_{HA} f_{HA,\infty}^{excel}/\rho_{fl} + f_{fl,\infty}^{excel}} \right]}{(1 - f_{exfib,0}^{excel}) \times \left[1 + (\rho_{HA}/\rho_{fl} - 1) \times f_{HA,\infty}^{excel} \right]}, \quad (33)$$

624 with

$$625 \quad f_{exfib,0}^{excel} = 1 - \frac{1}{0.88} \left(\frac{d_{max}}{d_{dry}} \right)^2 \frac{f_{col,\infty}^{excel}}{\rho_{HA} f_{HA,\infty}^{excel}/\rho_{fl} + f_{fl,\infty}^{excel} + f_{col,\infty}^{excel}}, \quad (34)$$

626 where $d_{max} = 1.52$ nm and $d_{dry} = 1.09$ nm, and with dependencies $f_{HA,\infty}^{excel}$, $f_{col,\infty}^{excel}$,
 627 and $f_{fl,\infty}^{excel}$ on tissue mass density as given in Sect. 3 (see Eqs. (16) and (17)).

628 In case of partially dehydrated tissues, some fluid mass (and corresponding vol-
 629 ume) will be lost during dehydration,

$$630 \quad \Delta f_{fl,\infty}^{\mu,dh} = f_{fl,\infty}^{\mu} - f_{fl,\infty}^{\mu,dh} = f_{fl,\infty}^{\mu} - \mathcal{R}^{\infty,dh} f_{col,\infty}^{\mu} \rho_{col}/\rho_{fl}, \quad (35)$$

631 with $\mathcal{R}^{\infty,dh}$ as the experimentally measured water-to-organic mass ratio of partially
 632 dehydrated tissues at the macroscopic scale, as e.g. given by Lees and Mook [89].

633 The volume fraction of the remaining fluid after dehydration per extracellular bone
634 matrix reads as

$$635 \quad f_{fl,\infty}^{excel,dh} = \frac{f_{fl,\infty}^{\mu} - \min(\Delta f_{fl,\infty}^{\mu,dh}, f_{\mu por})}{1 - f_{\mu por}}. \quad (36)$$

636 The lost fluid volume fraction in the extracellular scale amounts to

$$637 \quad \Delta f_{fl,\infty}^{excel,dh} = f_{fl,\infty}^{excel} - f_{fl,\infty}^{excel,dh}. \quad (37)$$

638 The mass density-diffraction spacing relation for partially dehydrated tissues reads
639 as

$$640 \quad d_{w,\infty}^{dh} = d_{w,\infty} \sqrt{1 - \frac{\Delta f_{fl,\infty}^{excel,dh} - f_{exfib,0}^{excel} \Delta f_{fl,\infty}^{excel,dh} / (1 - f_{col,0}^{excel})}{f_{fib,\infty}^{excel}}}, \quad (38)$$

641 with

$$642 \quad f_{fib,\infty}^{excel} = 1 - \left\{ \frac{f_{exfib,0}^{excel}}{1 + (\rho_{HA} / \rho_{fl} - 1) \times f_{HA,\infty}^{excel}} + \frac{f_{exfib,0}^{excel}}{1 - f_{col,0}^{excel}} \times (1 - \rho_{HA} / \rho_{fl}) \times f_{HA,\infty}^{excel} \right\}, \quad (39)$$

643 and

$$644 \quad f_{col,0}^{excel} = \frac{f_{col,\infty}^{excel}}{\rho_{HA} f_{HA,\infty}^{excel} / \rho_{fl} + f_{fl,\infty}^{excel} + f_{col,\infty}^{excel}}. \quad (40)$$

645 Identification of $\Delta f_{fl,\infty}^{excel,dh} = f_{fl,\infty}^{excel}$ delivers model predictions for the diffraction
646 spacings in fully dried tissues. These mass density-diffraction spacing relations are
647 fed with experimental data for tissue mass density and the corresponding predictions
648 for diffraction spacing are validated through comparison with experimental results
649 [87, 89, 93]. Very low prediction errors of $1.8 \pm 3.1\%$ underline the relevance of the
650 model-predicted evolutions of the tissue compartment volumes, and of the model-
651 predicted volume fractions during the mineralization process in different bone tissues
652 (see Fig. 12); and hence, the idea of hydroxyapatite precipitating under closed ther-
653 modynamic conditions from an ionic solution in the fibrillar and extrafibrillar spaces
654 of bone tissue. Accordingly, the structural (volumetric) evolution of mineralizing
655 bone tissue can be quantified as follows: during mineralization, the volume of the
656 overall collagenous tissue is shrinking because the mass density of hydroxyapatite
657 is around three times larger than that of liquid ionic solution. In general, the more
658 mineral is present in the tissue, the higher the shrinkage of the volumes of the dif-
659 ferent compartments (see Fig. 13). More specifically, this volume loss is minimal for
660 low-mineralized tissues at the beginning of the mineralization process (see the left
661 lower corner of Fig. 13), whereas highly mineralized bone tissue has lost up to 60%
662 of its initial (osteoid) volume (see the right upper corner of Fig. 13).

663 The compositional evolution can be also quantified in terms of volume fractions:
664 the mineralization process leads to a slight increase of the fibrillar volume frac-

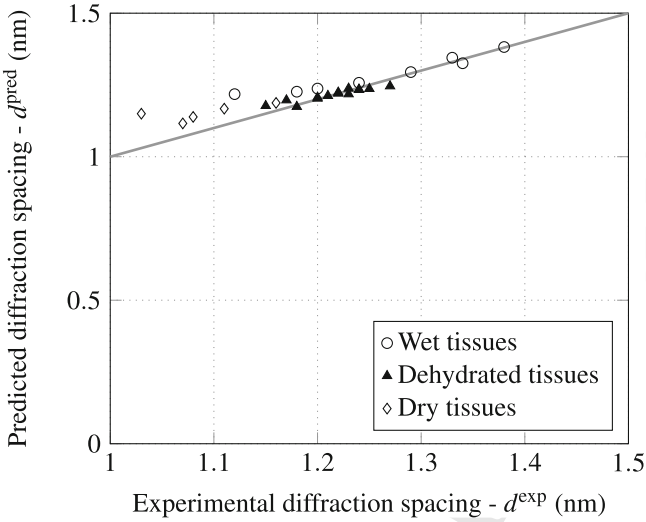


Fig. 12 Predicted versus experimental diffraction spacing for wet, dry, and partially dehydrated, mineralized tissues

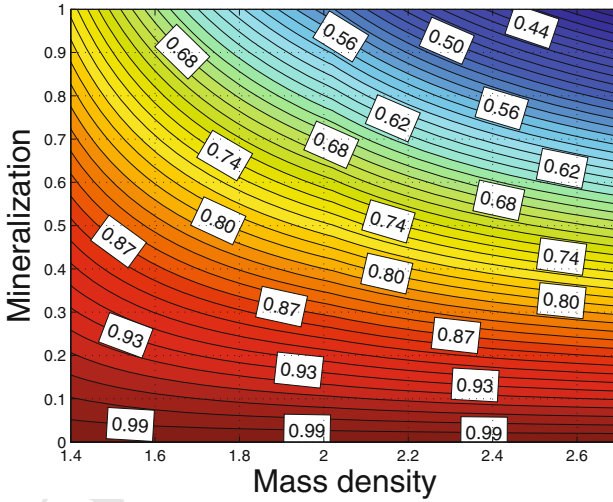


Fig. 13 Normalized tissue volume as function of the mineralization degree for different final tissue mass densities

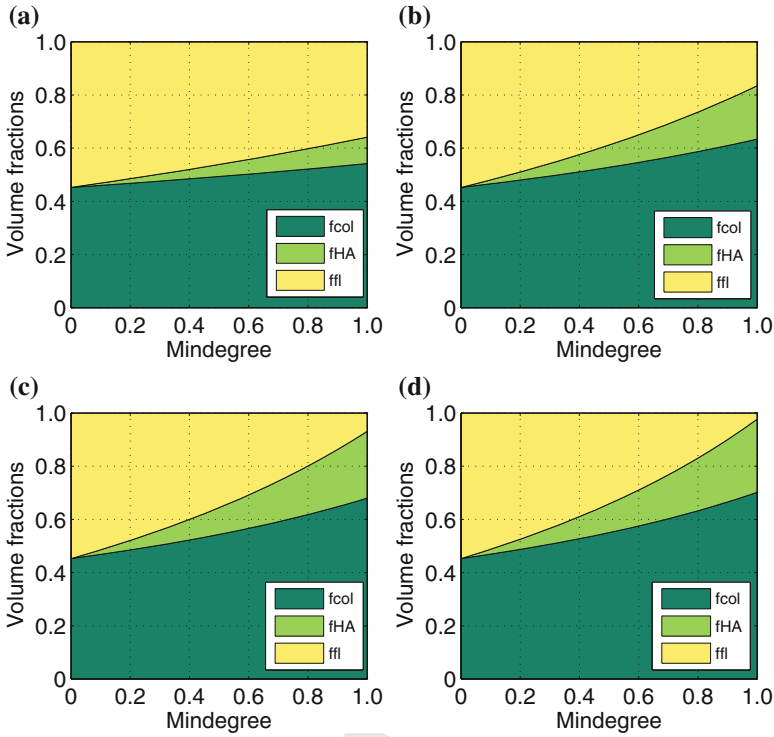


Fig. 14 Normalized tissue volume as function of the mineralization degree, for different final tissue mass densities

665 tions, since the fibrils, thanks to the presence of chemically inert collagen, are less
 666 affected by the fluid-to-crystal transformation-induced volume loss, as compared to
 667 the extrafibrillar space. Within the fibrils, the fluid volume fraction, starting from
 668 around 50% in the unmineralized osteoid, is reduced by one third in the case of
 669 low-mineralized tissues (see Fig. 14a), while it is almost completely consumed in
 670 the case of very highly mineralized tissues (see Fig. 14d). Thereby, lost fluid volume
 671 fractions are placed by collagen and mineral volume fractions, at about the same
 672 shares (see Fig. 14a–d). In the extrafibrillar space, mineral volume fractions increase
 673 overlinearly with the mineralization degree, the more so the more highly the tissue
 674 is mineralized.

7 Nano- and Microstructural Patterns Governing Anisotropic Tissue Elasticity

Throughout the last two decades, hierarchical material models for bone [4, 33, 53, 55, 56, 60, 61, 64–66, 98, 108, 110, 116, 118, 119, 124, 132, 154], developed within the frameworks of homogenization theory and continuum micromechanics [7, 37, 157] and validated through a multitude of biochemical, biophysical, and biomechanical experiments [13, 16, 25, 51, 57, 79, 86, 87, 90–92, 94, 96, 100, 126, 145], have opened the way to translate the chemical composition of extracellular bone material (i.e. the volume fractions of organics, water, and hydroxyapatite) into the tissue’s anisotropic elasticity. This section is devoted to briefly introducing the fundamentals of continuum micromechanics, and to presenting how this theoretical framework has elucidated the “construction plans” providing the most fascinating mechanical properties of bone.

Micromechanical Representation of Bone Tissue by Means of Representative Volume Elements (RVEs)

In continuum micromechanics [37, 71, 156, 157], a material is understood as a macro-homogeneous, but micro-heterogeneous body filling a representative volume element (RVE) with characteristic length ℓ , which must be both considerably larger than the dimensions of heterogeneities within the RVE, \mathbb{r} , and significantly smaller than the characteristic lengths of geometry or loading of a structure built up by the material defined on the RVE, \mathcal{L} . The characteristic length of structural loading typically coincides with wave lengths of signals traveling through the structure, or relates to macroscopic stress gradients according to $\mathcal{L} \approx \|\boldsymbol{\Sigma}\|/\|\text{GRAD}\boldsymbol{\Sigma}\|$ [7], with the “macroscopic” stress tensor $\boldsymbol{\Sigma}$. In mathematical terms, the aforementioned separation of scales requirement reads as

$$\mathbb{r} \ll \ell \ll \mathcal{L}. \quad (41)$$

Hereby, the first inequality sign typically relates to a factor of 2 to 3 [38]; while the second one typically relates to a factor of 5 to 50 [81].

In general, the microstructure within one RVE is so complex that it cannot be described in complete detail. Therefore, quasi-homogeneous subdomains, called material phases, with known physical quantities are reasonably chosen. Quantitative phase properties are volume fractions f_r of phases $r = 1, \dots, N_r$, (average) elastic properties, as well as the morphological description, as, e.g., the isotropy or the symmetries of anisotropy of the spatial distribution of the phases, the existence of one connected “matrix phase” in which one or several “inclusion phases” with different shapes are embedded (as in reinforced composite material), or the disordered arrangement of all phases (as in a polycrystal).

The central goal of continuum micromechanics is to estimate the mechanical properties (such as elasticity or strength) of the material defined on the RVE from the aforementioned phase properties. This procedure is referred to as homogenization or

one homogenization step. If a single phase exhibits a heterogeneous microstructure itself, its mechanical behavior can be estimated by introduction of an RVE within this phase [46], with dimensions $\ell_2 \leq \ell_1$, comprising again smaller phases with characteristic length $\ell_2 \ll \ell_1$, and so on, leading to a multistep homogenization scheme, as in case of bone (see Fig. 15). In this context, the following “universal” microstructural patterns are considered across the hierarchical organization of bone materials:

- an RVE of wet collagen, with a characteristic length of several nanometers (see Fig. 15a), represents the staggered organization of cylindrical collagen molecules (see Fig. 1h), which are attached to each other by ~ 1.5 nm long crosslinks [8, 93, 112]. These crosslinks imply the existence of a contiguous matrix built up by molecular collagen, hosting fluid-filled intermolecular spaces, which are represented by cylindrical inclusions;
- an RVE of extrafibrillar space (hydroxyapatite foam), with a characteristic length of several hundred nanometers (see Fig. 15c), hosts crystal needles (represented through infinitely many uniformly oriented cylindrical hydroxyapatite inclusions) oriented in all space directions; in mutual interaction with spherical, water-filled pores in-between;
- an RVE of extracellular bone matrix or ultrastructure, with a characteristic length of several micrometers (see Fig. 15d), hosts cylindrical, mineralized fibrils being embedded into a contiguous matrix built up by hydroxyapatite foam material;
- an RVE of extravascular bone material, with a characteristic length of several hundred micrometers (see Fig. 15e), hosts spherical, osteocyte-filled cavities called lacunae being embedded into a contiguous matrix built up by the extracellular bone material; and
- an RVE of cortical bone material, with a characteristic length of several millimeters (see Fig. 15f), hosts cylindrical vascular pores being embedded into a matrix of extravascular bone material.

Elasticity Homogenization

As concerns the homogenization (or upscaling) of the elastic properties of bone, starting from the level of its basic building blocks, up to the level of the bone microstructure, see Fig. 15, we start with focusing on a single RVE built up by phases enumerated by r . The second-order strain tensor, $\boldsymbol{\varepsilon}_r$, is related to the (average “microscopic”) second-order stress tensor in phase r , $\boldsymbol{\sigma}_r$, by the phase elasticity tensor \mathbb{C}_r

$$\boldsymbol{\sigma}_r = \mathbb{C}_r : \boldsymbol{\varepsilon}_r . \quad (42)$$

The RVE is subjected to homogeneous (macroscopic) strains \mathbf{E} at its boundary [59], prescribed in terms of displacements

$$\forall \mathbf{x} \in \partial V_{RVE} : \quad \boldsymbol{\xi}(\mathbf{x}) = \mathbf{E} \cdot \mathbf{x} , \quad (43)$$

whereby \mathbf{x} is the position vector for locations within or at the boundary of the RVE. As a consequence, the resulting kinematically compatible microstrains $\boldsymbol{\varepsilon}(\mathbf{x})$ throughout

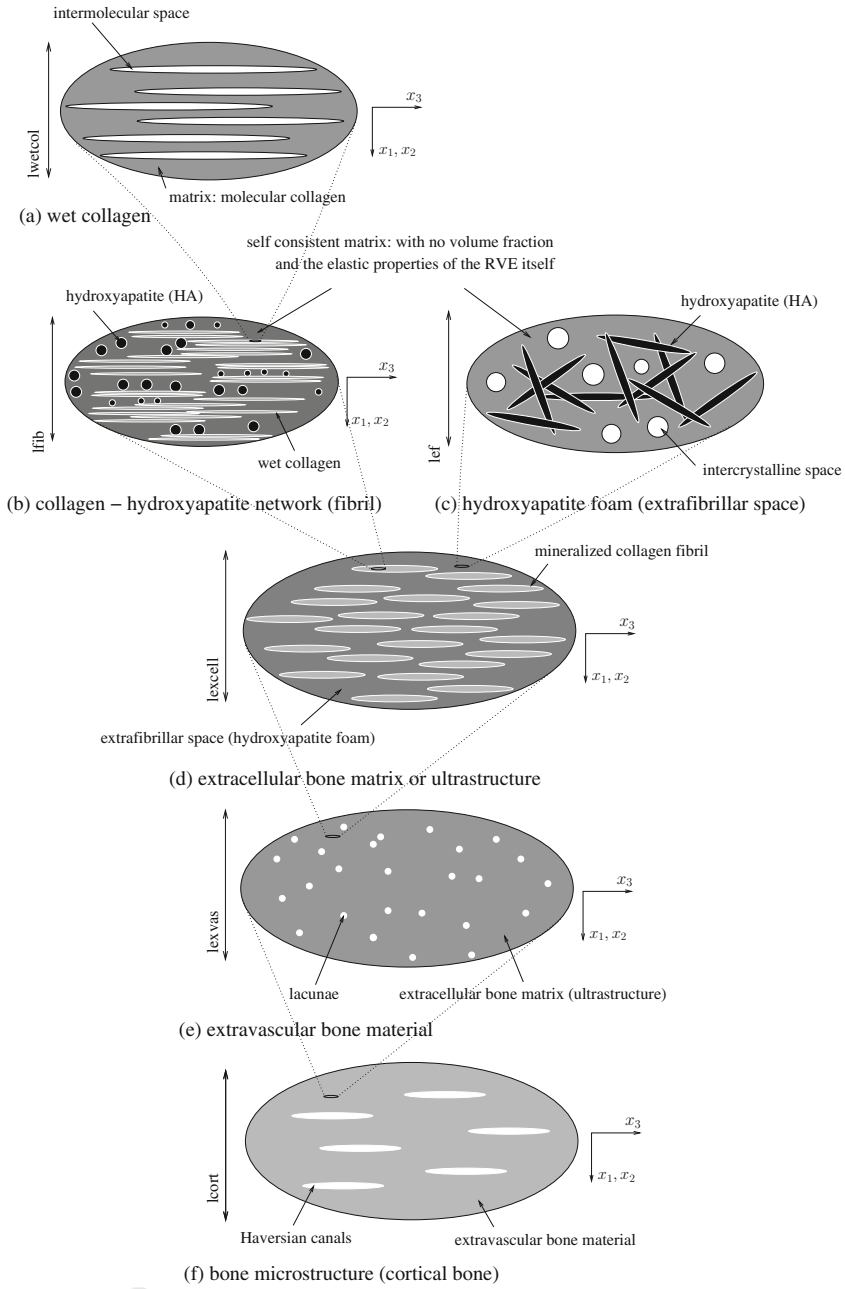


Fig. 15 Micromechanical representation of bone material by means of a six-step homogenization scheme, according to Fritsch et al. [48]

754 the RVE fulfill the average condition,

$$755 \quad \mathbf{E} = \frac{1}{V_{RVE}} \int_{V_{RVE}} \boldsymbol{\varepsilon} dV = \langle \boldsymbol{\varepsilon} \rangle = \sum_r f_r \boldsymbol{\varepsilon}_r, \quad (44)$$

756 providing link between the (average) microscopic and macroscopic strains. Further-
757 more, the aforementioned deformations provoke traction forces $\mathbf{T}(\mathbf{x})$ on the boundary
758 of the RVE, and microstresses $\boldsymbol{\sigma}(\mathbf{x})$ throughout the RVE, fulfilling the equilibrium
759 conditions

$$760 \quad \begin{aligned} \forall \mathbf{x} \in V_{RVE} \quad \operatorname{div} \boldsymbol{\sigma}(\mathbf{x}) &= \mathbf{0}, \\ \forall \mathbf{x} \in \partial V_{RVE} \quad \mathbf{T}(\mathbf{x}) &= \boldsymbol{\sigma}(\mathbf{x}) \cdot \mathbf{n}(\mathbf{x}), \end{aligned} \quad (45)$$

761 with $\mathbf{n}(\mathbf{x})$ as the normal to the boundary at position \mathbf{x} . The external work done by
762 these traction forces reads as

$$763 \quad \begin{aligned} \mathcal{W}^{ext} &= \int_{\partial V_{RVE}} \mathbf{T}(\mathbf{x}) \cdot \boldsymbol{\xi}(\mathbf{x}) dS = \int_{\partial V_{RVE}} (\mathbf{E} \cdot \mathbf{x}) \cdot [\boldsymbol{\sigma}(\mathbf{x}) \cdot \mathbf{n}(\mathbf{x})] dS \\ &= \mathbf{E} : \int_{V_{RVE}} \boldsymbol{\sigma}(\mathbf{x}) dV, \end{aligned} \quad (46)$$

764 whereby we made use of boundary condition (43) and of the divergence theorem.
765 Hence, the force quantity doing work on the macroscopic strains \mathbf{E} is the volume inte-
766 gral over the microscopic stress, which is independent of microscopic position and
767 of dimension “stress times volume”. This induces the existence of the macroscopic
768 stress $\boldsymbol{\Sigma}$ in the form

$$769 \quad \boldsymbol{\Sigma} V_{RVE} = \int_{V_{RVE}} \boldsymbol{\sigma}(\mathbf{x}) dV \Leftrightarrow \boldsymbol{\Sigma} = \frac{1}{V_{RVE}} \int_{V_{RVE}} \boldsymbol{\sigma}(\mathbf{x}) dV = \langle \boldsymbol{\sigma} \rangle = \sum_r f_r \boldsymbol{\sigma}_r, \quad (47)$$

771 i.e. the well-known stress average rule. Insertion of (47) into the principle of virtual
772 power [50, 99, 131], which in the case of linearized strains, can be expressed in
773 terms of an expression with the dimension “work”,

$$774 \quad \mathcal{W}^{ext} = -\mathcal{W}^{int} = \int_{V_{RVE}} \boldsymbol{\sigma}(\mathbf{x}) : \boldsymbol{\varepsilon}(\mathbf{x}) dV, \quad (48)$$

775 yields the so-called Hill’s lemma

$$776 \quad \boldsymbol{\Sigma} : \mathbf{E} = \frac{1}{V_{RVE}} \int_{V_{RVE}} \boldsymbol{\sigma}(\mathbf{x}) : \boldsymbol{\varepsilon}(\mathbf{x}) dV = \langle \boldsymbol{\sigma} : \boldsymbol{\varepsilon} \rangle. \quad (49)$$

777 Linearity of elastic law (42) and of partial differential equation (45)₁ imply a multi-
778 linear relation between the homogenized (macroscopic) strain \mathbf{E} and the average
779 (microscopic) strain $\boldsymbol{\varepsilon}_r$, expressed by the fourth-order concentration tensors \mathbb{A}_r of
780 each of the phases r ,

$$\boldsymbol{\varepsilon}_r = \mathbb{A}_r : \mathbf{E}. \quad (50)$$

Insertion of Eq. (50) into (42) and averaging over all phases according to Eq. (47) leads to

$$\boldsymbol{\Sigma} = \sum_r f_r \mathbb{C}_r : \mathbb{A}_r : \mathbf{E}. \quad (51)$$

Equation (51) implies the existence of a macroscopic ‘‘homogenized’’ stiffness tensor linking macroscopic stresses to macroscopic strains in the format

$$\boldsymbol{\Sigma} = \mathbb{C}^{\text{hom}} : \mathbf{E}, \quad (52)$$

yielding \mathbb{C}^{hom} as

$$\mathbb{C}^{\text{hom}} = \sum_r f_r \mathbb{C}_r : \mathbb{A}_r. \quad (53)$$

The concentration tensors \mathbb{A}_r are estimated from matrix-inclusion problems, pioneered by Eshelby [43]. On a mathematical level, this is achieved by setting the phase strains equal to those in ellipsoidal inclusions in infinitely extending matrices of stiffness \mathbb{C}^0 subjected to remote strains, and by combining respective semi-analytical relationships [43, 84] with stress and strain average rules [59, 157], yielding

$$\mathbb{A}_r = [\mathbb{I} + \mathbb{P}_r^0 : (\mathbb{C}_r - \mathbb{C}^0)]^{-1} : \left\{ \sum_s f_s [\mathbb{I} + \mathbb{P}_s^0 : (\mathbb{C}_s - \mathbb{C}^0)]^{-1} \right\}^{-1}. \quad (54)$$

Insertion of Eq. (54) into (51) yields an expression for the macroscopic homogenized stiffness tensor as function of their volume fractions, shapes and interactions

$$\mathbb{C}^{\text{hom}} = \sum_r f_r \mathbb{C}_r : [\mathbb{I} + \mathbb{P}_r^0 : (\mathbb{C}_r - \mathbb{C}^0)]^{-1} : \left\{ \sum_s f_s [\mathbb{I} + \mathbb{P}_s^0 : (\mathbb{C}_s - \mathbb{C}^0)]^{-1} \right\}^{-1}, \quad (55)$$

where f_r and \mathbb{C}_r are the volume fraction and the elastic stiffness of phase r , \mathbb{I} is the fourth-order unity tensor, \mathbb{P}_r^0 the fourth-order Hill tensor accounting for the characteristic shape of phase r , which, in case of ellipsoidal inclusions in anisotropic media [84, 85], reads as

$$P_{r,ijkl}^0 = \frac{1}{16\pi\alpha^{1/2}} \int_{\Omega} \frac{1}{t^3} \{ \hat{g}_{il} w_j w_k + \hat{g}_{ik} w_j w_l + \hat{g}_{jl} w_i w_k + \hat{g}_{jk} w_i w_l \} dS(\mathbf{w}). \quad (56)$$

In Eq. (56), the shape of the ellipsoid is considered by $\alpha = \det \alpha_{ij}$, being related to the equation of the ellipsoid, $\alpha_{ij} x_i x_j = 1$, $dS(\mathbf{w})$ is a surface element of the unit sphere (with surface Ω); w_1 , w_2 and w_3 are the components of the unit length vector \mathbf{w} pointing from the origin of the sphere to the surface element $dS(\mathbf{w})$, and

808 $t^2 = \alpha_{ij}^{-1} w_i w_j$. Finally, \hat{g}_{ik} are the components of the inverse of the second-order
 809 tensor $C_{ijkl}^0 w_j w_l$, with C_{ijkl}^0 denoting the stiffness of anisotropic matrix.

810 As regards the matrix stiffness, \mathbb{C}^0 , its choice governs the interactions between
 811 the phases inside the RVE: $\mathbb{C}^0 = \mathbb{C}^{\text{hom}}$ relates to a dispersed arrangement of phases
 812 where all phases “feel” the overall homogenized material, and the corresponding
 813 homogenization scheme is standardly called self-consistent [69, 83], well-suited for
 814 polycrystalline materials (applied for RVEs depicted in Fig. 15b, c). On the other
 815 hand, the matrix may be identified as a phase m itself, $\mathbb{C}^0 = \mathbb{c}_m$, which relates to
 816 matrix-inclusion-type composite, and the corresponding homogenization scheme is
 817 standardly referred to as Mori–Tanaka scheme [12, 106] (applied for RVEs depicted
 818 in Fig. 15a, d, e, f).

819 Strictly speaking, the RVE of extrafibrillar space (see Fig. 15c) requires a slight
 820 (but important) modification of the aforementioned developments: it consists of one
 821 pore space and infinitely many cylindrical solid phases which are oriented in all space
 822 directions. This requires modification of Eqs. (44), (47), (53), and (55) in terms of
 823 integrals over the unit sphere [47]. Accordingly, the homogenized stiffness of the
 824 extrafibrillar RVE of Fig. 15c reads as

$$\begin{aligned} \mathbb{C}_{\text{exfib}}^{\text{hom}} = & \left\{ f_{\text{HA}}^{\text{exfib}} \mathbb{C}_{\text{HA}} : \int_{\varphi=0}^{2\pi} \int_{\theta=0}^{\pi} \left[\mathbb{I} + \mathbb{P}_{\text{cyl}}^{\text{exfib}}(\theta, \varphi) : (\mathbb{C}_{\text{HA}} - \mathbb{C}_{\text{exfib}}^{\text{hom}}) \right]^{-1} \frac{\sin \theta d\theta d\varphi}{4\pi} + \right. \\ & \left. (1 - f_{\text{HA}}^{\text{exfib}}) \mathbb{C}_{\text{H}_2\text{O}} : \left[\mathbb{I} + \mathbb{P}_{\text{sph}}^{\text{exfib}} : (\mathbb{C}_{\text{H}_2\text{O}} - \mathbb{C}_{\text{exfib}}^{\text{hom}}) \right]^{-1} \right\} : \\ & \left\{ f_{\text{HA}} \int_{\varphi=0}^{2\pi} \int_{\theta=0}^{\pi} \left[\mathbb{I} + \mathbb{P}_{\text{cyl}}^{\text{exfib}}(\theta, \varphi) : (\mathbb{C}_{\text{HA}} - \mathbb{C}_{\text{exfib}}^{\text{hom}}) \right]^{-1} \frac{\sin \theta d\theta d\varphi}{4\pi} + \right. \\ & \left. (1 - f_{\text{HA}}^{\text{exfib}}) \left[\mathbb{I} + \mathbb{P}_{\text{sph}}^{\text{exfib}} : (\mathbb{C}_{\text{H}_2\text{O}} - \mathbb{C}_{\text{exfib}}^{\text{hom}}) \right]^{-1} \right\}^{-1}, \end{aligned} \quad (57)$$

825 with $\mathbb{P}_{\text{cyl}}^{\text{exfib}}$ and $\mathbb{P}_{\text{sph}}^{\text{exfib}}$ standing for the Hill tensor of a cylindrical or a spherical inclu-
 826 sion embedded in a matrix with a stiffness of $\mathbb{C}_{\text{exfib}}^{\text{hom}}$, respectively.

828 **Elasticity of Elementary Components**

829 The micromechanical representation of Fig. 15 is validated at different observa-
 830 tion scales, namely at the extracellular, the extravascular, and the cortical/trabecular
 831 scales. All corresponding computations are based on the *same* elasticity properties
 832 assigned to bone’s elementary constituents: hydroxyapatite, (molecular) collagen,
 833 and water (with some non-collagenous organics). The elastic properties of hydrox-
 834 yapatite are obtained from tests with an ultrasonic interferometer coupled with a
 835 solid media pressure apparatus [77], which reveal the isotropic elastic properties of
 836 hydroxyapatite powder,

$$837 \quad \mathbb{C}_{\text{HA}} = 3k_{\text{HA}} \mathbb{I}_{\text{vol}} + 2\mu_{\text{HA}} \mathbb{I}_{\text{dev}}, \quad (58)$$

with \mathbb{I}_{vol} and \mathbb{I}_{dev} as the volumetric and deviatoric part of the fourth-order identity tensor \mathbb{I} , and with $k_{\text{HA}} = 82.6 \text{ GPa}$ and $\mu_{\text{HA}} = 44.9 \text{ GPa}$, as the bulk and shear moduli of hydroxyapatite. In view of the largely disordered arrangement of poorly crystalline minerals [42, 45, 62, 63, 65, 95, 117], this isotropic characterization is sufficient for successful bone elasticity upscaling [33, 47, 61, 66, 154], as is also confirmed by the validation diagrams of Figs. 16, 17, 18, 19, 20 and 21. Sasaki and Odajima [133] determined the Young's modulus of molecular collagen by a hybrid mechanical–X-ray technique, considering Lees' 1987 packing model [86] for the cross-sectional arrangement of collagen molecules. This resulted in an elastic Young's modulus of 2.9 GPa. As they did not account for the additional 12% microporosity which is still present in "fully dehydrated" collagen [88], the aforementioned values relate to the RVE of Fig. 15a with 12% intermolecular space. Adopting a Poisson's ratio of 0.34 for such an RVE [35], the corresponding homogenization relation allows for back-analysis of an isotropic estimate of the stiffness tensor of molecular collagen, which reads in Kelvin–Mandel notation (see e.g. Eq. (44) of [68] or Eq. (2a) of [31]) as

$$\mathbb{C}_{\text{col}} = \begin{Bmatrix} 4.86 & 2.39 & 2.39 & 0 & 0 & 0 \\ 2.39 & 4.86 & 2.39 & 0 & 0 & 0 \\ 2.39 & 2.39 & 4.86 & 0 & 0 & 0 \\ 0 & 0 & 0 & 1.23 & 0 & 0 \\ 0 & 0 & 0 & 0 & 1.23 & 0 \\ 0 & 0 & 0 & 0 & 0 & 1.23 \end{Bmatrix} \text{ GPa}, \quad (59)$$

with a Young's modulus of 3.28 GPa and a Poisson's ratio of 0.33. We assign the standard bulk modulus of water, $k_{\text{H}_2\text{O}} = 2.3 \text{ GPa}$, to phases comprising water with mechanically insignificant amounts of non-collagenous organic matter.

Model Validation at the Extracellular Scale

At the extracellular level, we compare the micromechanical elasticity predictions to ultrasonic tests with 10 MHz frequency, performed on cortical bone samples of bovine, human, elephant, deer, cod, and dugong tissues [91, 92]. Given the measured wave velocities ranging from 2.38 to 4.18 km/s, the wave exhibited wave lengths between 238 and 418 μm , being by a factor of 23.8 to 41.8 larger than the RVE of Fig. 15d, hence they characterize the latter according to Eq. (41). As tissue-specific input values for the micromechanical model, the volume fractions entering the RVE descriptions of wet collagen (Fig. 15a), of the fibrillar and extrafibrillar spaces (Fig. 15b, c), and of the extracellular matrix (Fig. 15d) are needed.

As regards the cortical bone samples from bovine tibia [91], the macroscopic mass densities and weight fractions are given, see Table 1. Based on a typical microporosity of $f_{\mu\text{por}} = 5\%$, see our discussion around Eq. (9), the aforementioned quantities are transformed into ultrastructural (extracellular) weight fractions and apparent mass densities according to Eqs. (10)–(13), and into extracellular (ultrastructural) volume fractions according to Eqs. (16) and (17). Then, the mineral distribution rules of Sect. 4, and the swelling and shrinkage rules of Sect. 5 and 6 allow for quantification of the extrafibrillar and fibrillar volume fractions per volume of extracellular matrix as

Table 7 Experimental characterization of various cortical bone samples by Less et al. [91]^a, Less et al. [92]^b, and Less et al. [96]^c; Macroscopic and extracellular bone mass densities, ρ^μ and ρ^{excel} , longitudinal ultrasonic velocities in radial material directions, v_1 , experimental and model-predicted normal stiffness values in radial direction, C_{1111}^{exp} and C_{1111}^{pred} , respectively

Tissue	ρ^μ (g/cm ³)	ρ^{excel} (g/cm ³)	v_1 (km/s)	C_{1111}^{exp} (GPa)	C_{1111}^{pred} (GPa)
Bovine tibia ^a	2.02	2.07	3.18	21.0	24.1
Bovine tibia ^a	1.99	2.04	3.18	20.7	22.1
Bovine tibia ^a	1.95	2.00	3.18	20.2	19.7
Bovine tibia ^a	2.01	2.06	3.16	20.6	22.3
Bovine tibia ^a	2.04	2.09	3.27	22.4	21.7
Bovine tibia ^a	2.05	2.11	3.26	22.4	24.4
Bovine tibia ^b	2.07	2.13	3.32	23.4	25.7
Dugong rib ^b	2.02	2.07	3.00	18.7	22.5
Elephant radius ^b	1.94	1.99	3.05	18.5	18.1
Human femur ^b	1.93	1.98	3.13	19.4	17.6
Deer antler ^b	1.78	1.82	2.38	10.3	12.5
Deer antler ^b	1.74	1.78	2.40	10.2	11.5
Whale malleus ^c	2.49	2.49	4.85	58.6	57.2
Whale malleus ^c	2.53	2.53	4.89	60.5	61.8
Whale malleus ^c	2.51	2.51	4.55	52.0	59.4
Whale malleus ^c	2.45	2.45	4.61	52.1	52.8
Whale incus ^c	2.50	2.50	4.79	57.4	58.3
Whale incus ^c	2.46	2.46	4.70	54.3	53.9
Whale periotic ^c	2.40	2.40	4.15	41.3	47.7
Whale periotic ^c	2.48	2.48	4.60	52.5	56.0
Whale periotic ^c	2.50	2.50	4.53	51.3	58.3
Whale periotic ^c	2.52	2.52	4.65	54.5	60.6
Whale periotic ^c	2.58	2.58	4.84	60.4	67.9
Whale typamic bulla ^c	2.54	2.54	4.60	53.7	63.0
Whale typamic bulla ^c	2.50	2.50	4.53	51.3	58.3
Whale typamic bulla ^c	2.53	2.53	4.53	51.9	61.8
Whale typamic bulla ^c	2.54	2.54	4.54	52.4	63.0
Whale typamic bulla ^c	2.49	2.49	4.48	50.0	57.2

$$\begin{aligned}
 f_{\text{exfib}}^{\text{excel}} &= \frac{f_{\text{exfib},0}^{\text{excel}}}{1 + (\rho_{\text{HA}}/\rho_{\text{n}} - 1) \times f_{\text{HA}}^{\text{excel}}} + \frac{f_{\text{exfib},0}^{\text{excel}}}{1 - f_{\text{col},0}^{\text{excel}}} \times (1 - \rho_{\text{HA}}/\rho_{\text{n}}) \times f_{\text{HA}}^{\text{excel}}, \\
 f_{\text{fib}}^{\text{excel}} &= 1 - f_{\text{exfib}}^{\text{excel}},
 \end{aligned} \tag{60}$$

whereby $f_{\text{exfib},0}^{\text{excel}}$ and $f_{\text{col},0}^{\text{excel}}$ are determined from Eqs. (34) and (40), with $f_{\text{col},\infty}^{\text{excel}} = f_{\text{col}}^{\text{excel}}$ according to Eq. (18), with $f_{\text{HA},\infty}^{\text{excel}} = f_{\text{HA}}^{\text{excel}}$ according to Eqs. (16)₂ and (17)₂. They are the basis for the determination of the phase volume fractions within the lower scale RVEs: In this context, the fact that the average hydroxyapatite concentration in the extracollagenous space is the same inside and outside the fibrils [63], see also Sect. 4, allows for quantification of the mineral and collagen volume fractions within the fibrillar and extrafibrillar compartments. Accordingly, in the extrafibrillar space, the volume fractions of mineral, $f_{\text{HA}}^{\text{exfib}}$, and of the intercrystalline fluid, $f_{\text{ic}}^{\text{exfib}}$, read as [108]

$$\begin{aligned}
 f_{\text{HA}}^{\text{exfib}} &= \frac{f_{\text{HA}}^{\text{excel}} \phi_{\text{HA}}^{\text{exfib}}}{f_{\text{exfib}}^{\text{excel}}} \quad \text{with} \quad \phi_{\text{HA}}^{\text{exfib}} = \frac{1 - f_{\text{fib}}^{\text{excel}}}{1 - f_{\text{col}}^{\text{excel}}}, \\
 f_{\text{ic}}^{\text{exfib}} &= 1 - f_{\text{HA}}^{\text{exfib}}.
 \end{aligned} \tag{61}$$

Within the fibrillar space, the volume fractions of mineral, $f_{\text{HA}}^{\text{fib}}$, and of wet collagen, $f_{\text{wetcol}}^{\text{fib}}$ read as [108]

$$\begin{aligned}
 f_{\text{HA}}^{\text{fib}} &= \frac{f_{\text{HA}}^{\text{excel}} (1 - \phi_{\text{HA}}^{\text{exfib}})}{f_{\text{fib}}^{\text{excel}}}, \\
 f_{\text{wetcol}}^{\text{fib}} &= 1 - f_{\text{HA}}^{\text{fib}}.
 \end{aligned} \tag{62}$$

Finally, the volume fractions of molecular collagen and the intermolecular space at the wet collagen level, $f_{\text{col}}^{\text{wetcol}}$ and $f_{\text{im}}^{\text{wetcol}}$, can be calculated from the extracellular volume fractions of collagen as [108]

$$\begin{aligned}
 f_{\text{col}}^{\text{wetcol}} &= \frac{f_{\text{col}}^{\text{excel}}}{f_{\text{fib}}^{\text{excel}} f_{\text{wetcol}}^{\text{fib}}}, \\
 f_{\text{im}}^{\text{wetcol}} &= 1 - f_{\text{col}}^{\text{wetcol}}.
 \end{aligned} \tag{63}$$

The corresponding micromechanical elasticity predictions of the bovine tibial bone samples of Lees et al. [91] agree well with the actual experimental data. This is underlined by relative errors of $5.47 \pm 7.01\%$ for the radial normal stiffness, and of $-2.84 \pm 6.70\%$ for the axial normal stiffness components, see also Figs. 16 and 17.

As regards the wet cortical bone samples from deer antler, human femur, elephant radius, and dugong rib of Lees et al. [92], and the various whale bones of Lees et al. [96], the macroscopic mass densities are given, see Table 7. Based on a typical microstructural porosity of $f_{\mu\text{por}} = 5\%$, these macroscopic mass densities are transformed into ultrastructural (extracellular) mass densities, by means of Eq. (9). The

Table 8 Experimental characterization of various cortical bone samples by Less et al. [91]^a and Less et al. [92]^b; Macroscopic and extracellular bone mass densities, ρ^μ and ρ^{excel} , longitudinal ultrasonic velocities in axial material directions, v_3 , experimental and model-predicted normal stiffness values in axial direction, C_{3333}^{exp} and C_{3333}^{pred} , respectively

Tissue	ρ^μ (g/cm ³)	ρ^{excel} (g/cm ³)	v_3 (km/s)	C_{3333}^{exp} (GPa)	C_{3333}^{pred} (GPa)
Bovine tibia ^a	2.06	2.12	3.92	32.5	32.3
Bovine tibia ^a	2.05	2.11	3.92	32.4	31.6
Bovine tibia ^a	2.02	2.07	3.81	30.1	27.3
Bovine tibia ^a	2.02	2.07	3.86	30.9	27.6
Bovine tibia ^a	2.00	2.05	3.90	31.2	28.3
Bovine tibia ^a	2.05	2.11	3.88	31.7	30.7
Bovine tibia ^a	2.10	2.16	3.88	32.5	35.4
Bovine tibia ^a	2.08	2.14	3.92	32.8	33.8
Bovine tibia ^b	2.06	2.12	4.18	37.0	34.3
Elephant radius ^b	1.93	1.98	3.89	29.9	23.5
Human femur ^b	1.96	2.01	3.76	28.4	25.8
Deer antler ^b	1.74	1.78	3.08	16.9	13.1
Deer antler ^b	1.73	1.77	3.15	17.5	12.8

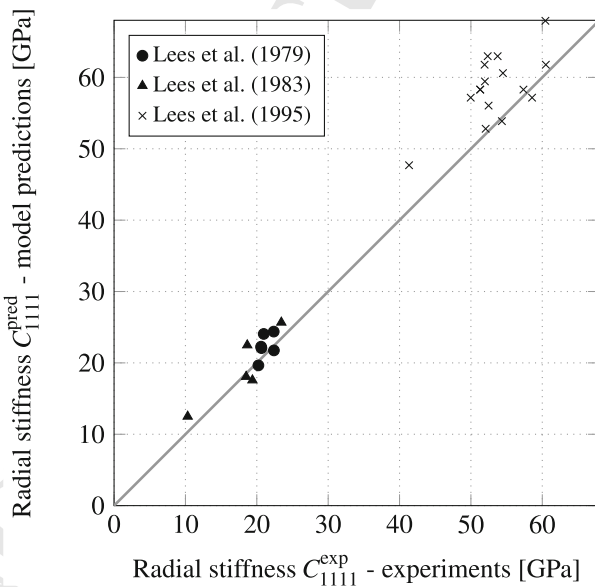


Fig. 16 Comparison between model predictions and experiments of radial normal stiffness values at the extracellular scale (10 MHz experiments: Lees et al. [91, 92, 96], see also Table 7)

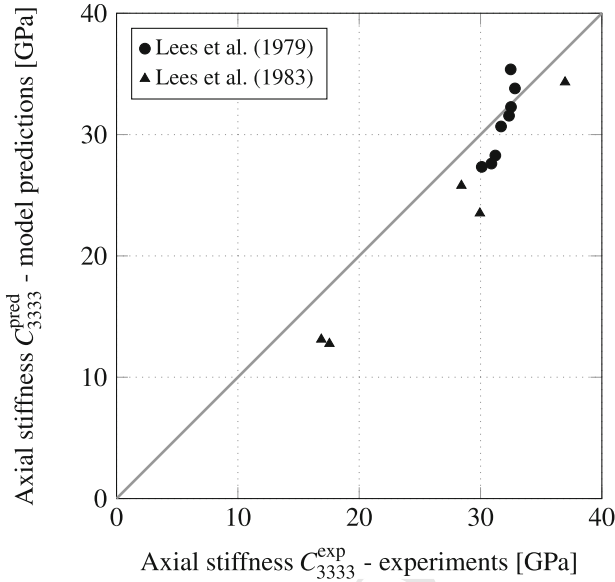


Fig. 17 Comparison between model predictions and experiments of axial normal stiffness values at the extracellular scale (10MHz experiments: Lees et al. [91, 92], see also Table 8)

901 latter mass densities then enter the bilinear relation of Fig. 2a, so as to deliver the
 902 extracellular volume fractions of mineral, organic and water according to Eqs. (16)
 903 and (17). These volume fractions are then used to quantify the composition of the
 904 lower scale RVEs of Fig. 1d, e. The corresponding micromechanical elasticity pre-
 905 dictions of the bone samples of Lees et al. [92] and of Lees et al. [96] agree well
 906 with the actual experimental data. This is underlined by relative errors of $7.18 \pm$
 907 12.13% for the radial normal stiffness, and of $-15.61 \pm 6.17\%$ for the axial normal
 908 stiffness components for the different bone tissues reported by Lees et al. [92], and
 909 by a relative error of $9.71 \pm 7.21\%$ for the radial normal stiffness of whale bones
 910 reported by Lees et al. [96], see Figs. 16 and 17.

911 *Model Validation at the Extravascular Scale*

912 At the extravascular level, we compare the micromechanical elasticity predictions
 913 to an ultrasonic test carried out by McCarthy et al. [100] on equine bones; at a fre-
 914 quency of 2.25 MHz. The measured velocities range from 3.13 to 4.4 km/s, resulting
 915 in a wave length ranging from 1.4 to 2.0 mm. The characteristic length of exper-
 916 imentally characterized RVE of Fig. 15e is by a factor of 14 to 20 smaller, hence
 917 they characterize the latter according to Eq. (41). As tissue-specific input values for
 918 the micromechanical model, the volume fractions entering the RVE descriptions of
 919 wet collagen (Fig. 15a), of the fibrillar and extrafibrillar spaces (Fig. 15b, c), of the
 920 extracellular matrix (Fig. 15d), and of the extravascular matrix (Fig. 15e) are needed.

Table 9 Experimental characterization of equine cortical bone samples by McCarthy et al. [100]; Macroscopic and extravascular bone mass densities, ρ^μ and ρ^{exvas} , longitudinal ultrasonic velocities in radial and axial material directions, v_1 and v_3 , experimental and model-predicted normal stiffness values in radial and axial direction, C_{1111}^{exp} , C_{3333}^{exp} , C_{1111}^{pred} , C_{3333}^{pred} , respectively

ρ^μ (g/cm ³)	ρ^{exvas} (g/cm ³)	v_1 (km/s)	v_3 (km/s)	C_{1111}^{exp} (GPa)	C_{3333}^{exp} (GPa)	C_{1111}^{pred} (GPa)	C_{3333}^{pred} (GPa)
2.03	2.14	3.60	4.30	27.8	39.7	27.4	37.5
2.02	2.11	3.55	4.20	26.6	37.2	25.1	34.3
2.01	2.13	3.45	4.10	25.4	35.9	26.8	36.6
2.01	2.09	3.65	4.40	27.8	40.4	23.7	32.4
2.00	2.10	3.55	4.20	26.5	37.0	24.5	33.5
2.00	2.08	3.40	4.20	24.0	36.6	23.1	31.5
2.00	2.06	3.58	4.30	26.5	38.2	22.4	30.5
1.98	2.11	3.42	4.10	24.7	35.5	25.4	34.8
1.98	2.11	3.35	4.15	23.7	36.4	25.4	34.8
1.98	2.09	3.50	4.15	25.6	36.0	23.9	32.6
1.98	2.09	3.60	4.30	27.1	38.6	23.9	32.6
1.97	2.08	3.50	4.03	25.5	33.7	23.2	31.7
1.97	2.10	3.35	4.20	23.6	37.1	24.7	33.8
1.96	2.08	3.50	4.03	25.5	33.8	23.3	31.8
1.96	2.07	3.60	4.20	26.8	36.5	22.6	30.8
1.95	2.10	3.52	3.95	26.1	32.8	24.9	34.0
1.95	2.04	3.40	4.03	23.6	33.2	21.3	28.9
1.95	2.08	3.35	4.10	23.3	35.0	23.3	31.8
1.95	2.16	3.42	4.10	25.2	36.3	28.4	38.8
1.95	2.07	3.45	4.15	24.6	35.6	22.6	30.8
1.95	2.10	3.55	4.15	26.5	36.2	24.9	34.0
1.93	2.06	3.35	4.03	23.1	33.4	22.0	30.0
1.93	2.02	3.30	4.10	22.0	34.0	20.1	27.2
1.93	2.07	3.48	4.25	25.1	37.4	22.7	31.0
1.92	2.05	3.35	4.00	23.0	32.7	21.4	29.1
1.92	2.02	3.40	4.03	23.4	32.8	20.1	27.2
1.92	2.05	3.35	4.20	23.0	36.1	21.4	29.1
1.92	2.03	3.40	4.20	23.5	35.9	20.7	28.1
1.91	2.03	3.35	4.13	22.8	34.7	20.7	28.2
1.91	2.17	3.48	4.17	26.2	37.7	29.0	39.5
1.91	2.11	3.45	4.35	25.1	39.9	25.2	34.4
1.90	2.20	3.13	3.95	21.6	34.3	31.3	42.7
1.90	2.02	3.40	4.00	23.4	32.4	20.1	27.3
1.82	1.90	3.30	4.00	20.7	30.4	14.9	18.9
1.76	2.09	3.20	3.85	21.4	30.9	23.7	32.4

McCarthy et al. [100] reported the macroscopic mass densities, ρ^μ , and the vascular porosities f_{vas} , which give access, based on the typical lacunar and canalicular porosities of 1.3% and 0.7%, respectively, to the extravascular and extracellular mass densities, ρ^{exvas} and ρ^{excel} . The latter enters the bilinear relations given by Eqs. (16) and (17), delivering the extracellular volume fractions of hydroxyapatite, collagen and water. The volume fractions of the lower scale RVEs of Fig. 15 follow from Eqs. (60)–(63). The corresponding micromechanical elasticity prediction of the equine metacarpal bone samples of McCarthy et al. [100] agree well with the actual experimental data. This is underlined by relative errors of $-4.23 \pm 11.33\%$ for the radial normal stiffness, and of $-9.78 \pm 10.52\%$ for the axial normal stiffness components, see Fig. 18.

In order to check the predictive capabilities of the micromechanical model concerning the off-diagonal and shear stiffness components of the elasticity tensor, we consider the stiffness tensor given by Ashman et al. [6] on the basis of 2.25 MHz ultrasonic tests on human femoral samples, reading in Kelvin–Mandel notation (see e.g. Eq. (44) of Helnwein [68] or Eq. (20) of Cowin [31]) as

$$\mathbb{C}^{exp} = \begin{Bmatrix} 18.0 & 9.98 & 10.1 & 0 & 0 & 0 \\ 9.98 & 20.2 & 10.7 & 0 & 0 & 0 \\ 10.1 & 10.7 & 27.6 & 0 & 0 & 0 \\ 0 & 0 & 0 & 12.46 & 0 & 0 \\ 0 & 0 & 0 & 0 & 11.22 & 0 \\ 0 & 0 & 0 & 0 & 0 & 9.04 \end{Bmatrix} \quad \text{GPa.} \quad (64)$$

It should be noted that Ashman et al. [6] use macroscopic mass density values for the evaluation of the ultrasonic velocity measurements, while 2.25 MHz, as stated previously, actually refer to the extravascular RVE of Fig. 1d. Accordingly, the values given in (64) need to be corrected by a factor of

$$\frac{\rho^{exvas}}{\rho^\mu} = \frac{\rho^\mu - \rho_{H_2O} f_{vas}}{(1 - f_{vas})\rho^\mu} = 1.04 \quad (65)$$

taking $\rho^\mu = 1.90 \text{ g/cm}^3$ from the tests of Ashman et al. [6]. Considering a typical vascular porosity of 8% in human femoral bone [19, 20, 30, 36, 140], yields

$$\mathbb{C}_{exvas}^{exp} = \begin{Bmatrix} 18.74 & 10.39 & 10.52 & 0 & 0 & 0 \\ 10.39 & 21.03 & 11.14 & 0 & 0 & 0 \\ 10.52 & 11.14 & 28.74 & 0 & 0 & 0 \\ 0 & 0 & 0 & 12.97 & 0 & 0 \\ 0 & 0 & 0 & 0 & 11.68 & 0 \\ 0 & 0 & 0 & 0 & 0 & 9.41 \end{Bmatrix} \quad \text{GPa.} \quad (66)$$

Applying the mass-density based volume fraction evaluation procedure to the same human femur sample provided by Ashman et al. [6] delivers the volume fractions entering the RVEs at all scales of Fig. 15. Based on a microporosity of $f_{\mu por} =$

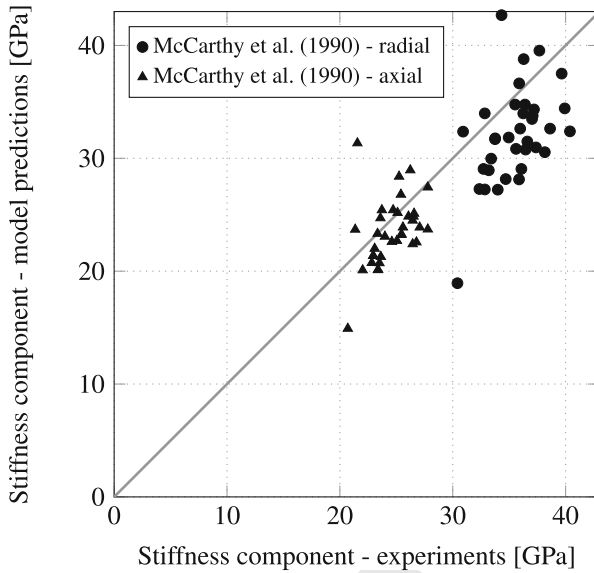


Fig. 18 Comparison between model predictions and experiments of radial and axial normal stiffness values at the extravascular scale (2.25 MHz experiments: McCarthy et al. [100], see also Table 9)

949 **10%** in consistency with the vascular porosity value given further above and the
 950 lacunar and canalicular porosities given below Eq. (8), the macroscopic mass density
 951 $\rho^\mu = 1.90 \text{ g/cm}^3$ is translated into an extracellular mass density entering Eq. (16).
 952 The volume fractions of the lower scale RVEs then follow from Eqs. (61)–(63). The
 953 corresponding micromechanical model prediction reads as

$$954 \quad \mathbb{C}_{\text{exvas}}^{\text{pred}} = \begin{Bmatrix} 17.71 & 6.88 & 6.76 & 0 & 0 & 0 \\ 6.88 & 17.71 & 6.76 & 0 & 0 & 0 \\ 6.76 & 6.76 & 23.92 & 0 & 0 & 0 \\ 0 & 0 & 0 & 11.09 & 0 & 0 \\ 0 & 0 & 0 & 0 & 11.09 & 0 \\ 0 & 0 & 0 & 0 & 0 & 9.68 \end{Bmatrix} \text{ GPa.} \quad (67)$$

955 The satisfactory agreement between model prediction and experimental data is underlined by an absolute error of $-9.13 \pm 7.8\%$ for the diagonal stiffness components.
 956 The off-diagonal stiffness components are less well predicted; however, these components are particularly prone to experimental errors, see e.g. [44, 80, 82, 114].

959 **Model Validation at the Macroscopic Scale**

960 At the trabecular level, we compare the micromechanical elasticity predictions to ultrasonic tests [126, 145] on bovine femoral and human tibial tissues; at a frequency of 50 kHz, as well as to mechanical tests of Keaveny et al. [79] on bovine tibial tissue samples. Given a typical wave propagation velocity of 3 km/s in the tested bone

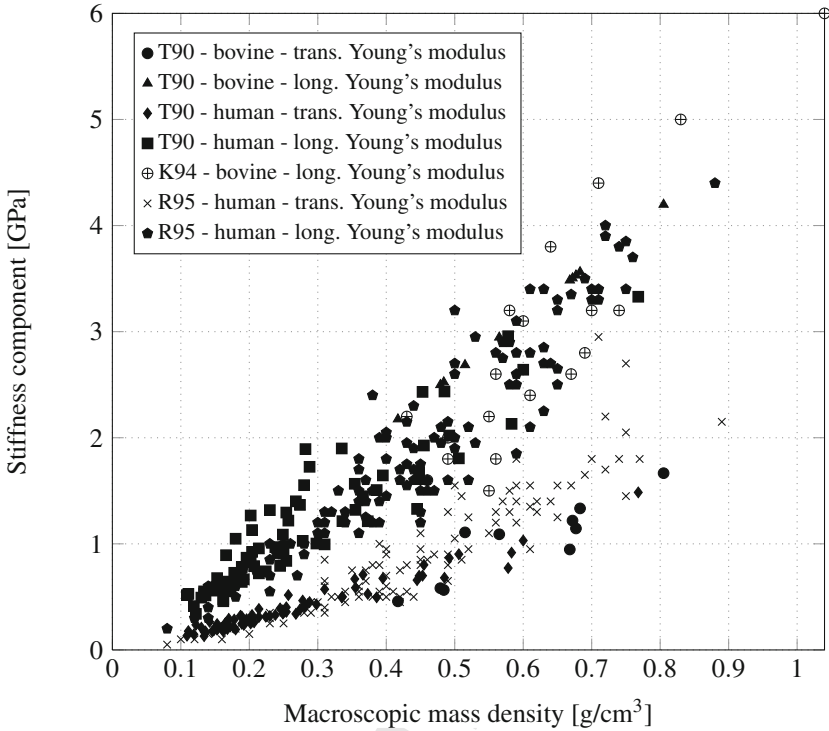


Fig. 19 Experimental data used for model validation: Macroscopic elastic stiffness constants of trabecular bone as a function of macroscopic mass density ρ^μ ; T90...[145], K94... [79], R95... [126]

964 specimens, the characteristic wave length was of the order of 6 cm, being by a factor
 965 of 60 larger than the RVE of Fig. 15f, hence they characterize the latter according to
 966 Eq. (41). As tissue-specific input values for the micromechanical model, the volume
 967 fractions entering the RVE descriptions of wet collagen (Fig. 15a), of the fibrillar
 968 and extrafibrillar spaces (Fig. 15b, c), of the extracellular matrix (Fig. 15d), of the
 969 extravascular matrix (Fig. 15e), and of the bone microstructure (Fig. 15f) are needed.

970 For marrow-cleared trabecular bone, as tested by Keaveny et al. [79], Rho et al.
 971 [126], Turner et al. [145], the corresponding volume fractions can be derived from
 972 the measured macroscopic mass density, ρ^μ , see Fig. 19. For the extravascular mass
 973 density of bone, we take $\rho^{exvas} = 1.74 \text{ g/cm}^3$ for bovine, and $\rho^{exvas} = 1.76 \text{ g/cm}^3$ for
 974 human bone specimens [5]. Assuming that the lacunar-canalicular volume fraction
 975 per extravascular bone, $f_{lac+can}^{exvas} = 0.021$, is the same in cortical and trabecular bone,
 976 the extracellular mass density follows from

$$977 \quad \rho^{excel} = \frac{\rho^{exvas} - \rho_{H_2O} \times f_{lac+can}^{exvas}}{1 - f_{lac+can}^{exvas}}. \quad (68)$$

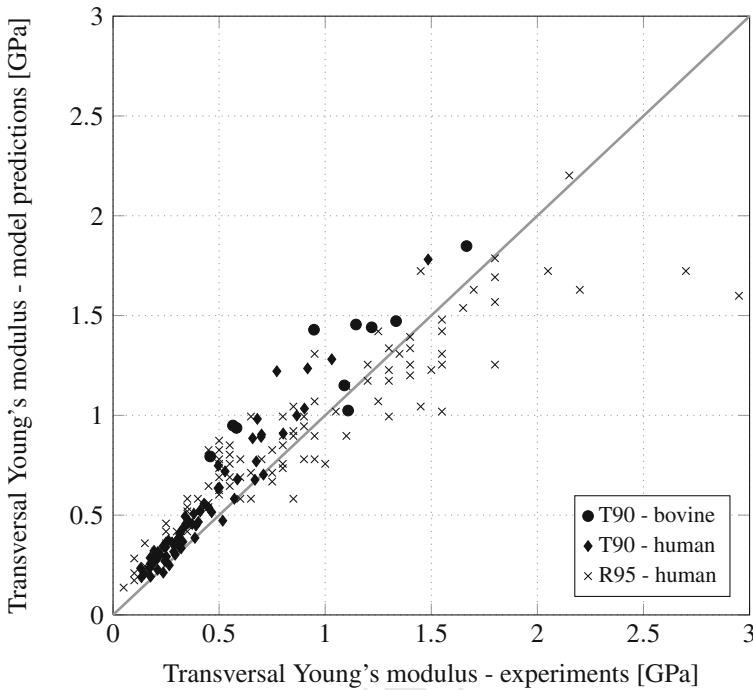


Fig. 20 Comparison between model predicted and experimental macroscopic elastic stiffness constants of trabecular bone in transverse direction (50kHz ultrasonic and mechanical experiments); T90...[145], K94... [79], R95... [126]

978 The sought volume fractions can be computed from Eqs. (16), (17) and (60)–(63). The
 979 relative errors of the corresponding micromechanical elasticity predictions amount
 980 to $23.62 \pm 16.75\%$ in radial, and $23.39 \pm 30.83\%$ in axial direction for the bovine
 981 samples of Turner et al. [145]; $24.67 \pm 20.72\%$ in radial, and $31.45 \pm 25.45\%$ in
 982 axial direction for the human samples of Turner et al. [145]; $12.72 \pm 21.40\%$ in radial
 983 direction for the bovine samples of Keaveny et al. [79]; and $0.09 \pm 28.44\%$ in radial,
 984 and $28.26 \pm 17.03\%$ in axial direction for the human samples of Rho et al. [126],
 985 see Figs. 20 and 21.

986 8 Concluding Remarks

987 Multiscale homogenization schemes similar to the one of Fig. 15 can also be
 988 employed for successful upscaling of mechanical properties of bone beyond the realm
 989 of elasticity. This was reported for poroelasticity [60, 64, 67, 108], for strength [48],
 990 and for viscoelasticity [40]. While we refer to the aforementioned references concern-
 991 ing experimental data bases used for micromechanics model validation, we note

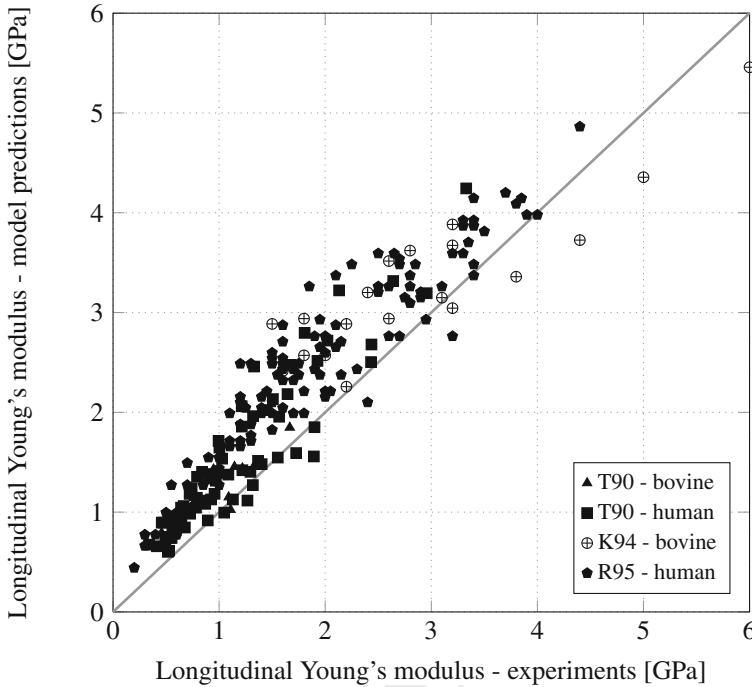


Fig. 21 Comparison between model predicted and experimental macroscopic elastic stiffness constants of trabecular bone in longitudinal direction (50 kHz ultrasonic and mechanical experiments); T90...[145], K94... [79], R95... [126]

992 in passing that a satisfactory performance of the strength and viscoelastic upscaling
 993 schemes stems from the consideration of sliding processes between the nanoscaled
 994 mineral crystals. This is in line with ongoing discussions in the bone materials science
 995 at large, be it in the context of Mohr-Coulomb-type, non-granular behavior elucidated
 996 by nanoindentation and atomic force microscopy [141]; or in the context of
 997 interface nanomechanics cast in the framework of molecular dynamics simulations
 998 [123]. The aforementioned poromechanics approaches are particularly valuable for
 999 quantifying the mechanical state in the vascular and lacunar pore spaces when the
 1000 biological cells reside, i.e. the oscillating hydrostatic pressure to which they respond
 1001 in a chemical fashion, see [136] and references therein. They also provide a natural
 1002 link between micromechanics on the one hand, and system biology and cell population
 1003 models on the other hand [134, 135]. This results in a rather “rigorously” derived
 1004 “mechano-biology of bone”. Finally, multiscale micromechanics models can be readily
 1005 combined with physics results, then allowing for the in-depth use and evaluation
 1006 of clinical X-ray data from Computed Tomography yielding micromechanics-based
 1007 Finite Element models at the organ scale. The latter elucidates the fascinating load
 1008 carrying behavior of these organs, and also pave the way to patient-specific bone
 1009 fracture risk assessment [14, 15].

References

- 1010
- 1011 1. J. Aaron, Histology and micro-anatomy of bone, in *Calcium, Phosphate and Magnesium*
- 1012 *Metabolism: Clinical Physiology and Diagnostic Procedures*, ed. by B.E.C. Nordin (Churchill
- 1013 Livingstone, New York, 1971), pp. 298–356
- 1014 2. B. Alexander, T.L. Daulton, G.M. Genin, J. Lipner, J.D. Pasteris, B. Wopenka, S. Thomopoulos,
- 1015 The nanometre-scale physiology of bone: steric modelling and scanning transmission
- 1016 electron microscopy of collagen-mineral structure. *J. R. Soc. Interface* **9**, 1774–1786 (2012)
- 1017 3. H.C. Anderson, The role of matrix vesicles in growth plate development and biomineralization.
- 1018 *Front. Biosci.* **10**, 822–837 (2005)
- 1019 4. B. Aoubiza, J.M. Crolet, A. Meunier, On the mechanical characterization of compact bone
- 1020 structure using the homogenization theory. *J. Biomech.* **29**(12), 1539–1547 (1996)
- 1021 5. R.B. Ashman, J. Rho, Elastic modulus of trabecular bone material. *J. Biomech.* **21**(3), 177181
- 1022 (1988)
- 1023 6. R.B. Ashman, S.C. Cowin, W.C. van Buskirk, J.C. Rice, A continuous wave technique for
- 1024 the measurement of the elastic properties of cortical bone. *J. Biomech.* **17**(5), 349361 (1984)
- 1025 7. J.-L. Auriault, C. Boutin, C. Geindreau, *Homogenization of Coupled Phenomena in Heterogeneous*
- 1026 *Media* (Wiley, New York, 2009)
- 1027 8. A.J. Bailey, R.G. Paul, L. Knott, Mechanisms of maturation and ageing of collagen. *Mech.*
- 1028 *Ageing Dev.* **106**(1–2), 1–56 (1998)
- 1029 9. Y. Bala, D. Farlay, P. Delmas, P. Meunier, G. Boivin, Time sequence of secondary mineralization
- 1030 and microhardness in cortical and cancellous bone from ewes. *Bone* **46**, 1204–1212
- 1031 (2010)
- 1032 10. D. Baylink, J. Wergedal, Bone formation and resorption by osteocytes, (1971), pp. 257–289
- 1033 11. L.S. Bell, M. Kayser, C. Jones, The mineralized osteocyte: a living fossil. *Am. J. Phys.*
- 1034 *Anthropol.* **137**, 449–456 (2008)
- 1035 12. Y. Benveniste, A new approach to the application of Mori–Tanaka’s theory in composite
- 1036 materials. *Mech. Mater.* **6**(2), 147–157 (1987)
- 1037 13. R. Biltz, E. Pellegrino, The chemical anatomy of bone. *J. Bone Joint Surg.* **51–A**(3), 456–466
- 1038 (1969)
- 1039 14. R. Blanchard, A. Dejaco, E. Bongaers, C. Hellmich, Intravoxel bone micromechanics for
- 1040 microCT-based finite element simulations. *J. Biomech.* **46**, 2710–2721 (2013)
- 1041 15. R. Blanchard, C. Morin, A. Malandrino, A. Vella, S. Zdenka, C. Hellmich, Patient-specific
- 1042 fracture risk assessment of vertebrae: a multiscale approach coupling X-ray physics and
- 1043 continuum micromechanics. *Numer. Methods Biomed. Eng.* **32**(9), XX (2016)
- 1044 16. L.C. Bonar, S. Lees, H.A. Mook, Neutron diffraction studies of collagen in fully mineralized
- 1045 bone. *J. Mol. Biol.* **181**(2), 265–270 (1985)
- 1046 17. L. Bonewald, M. Johnson, Osteocytes, mechanosensing and Wnt signaling. *Bone* **42**(4), 606–
- 1047 615 (2008)
- 1048 18. E. Bonucci, The osteocyte: the underestimated conductor of the bone orchestra. *Rend. Lincei*
- 1049 *Sci. Fis. e Nat.* **20**, 237–254 (2009)
- 1050 19. V. Bousson, C. Bergot, A. Meunier, F. Barbot, C. Parlier-Cuau, A.-M. Laval-Jeantet, J.-D.
- 1051 Laredo, CT of the middiaphyseal femur: cortical bone mineral density and relation to porosity.
- 1052 *Radiology* **217**(1), 179–187 (2000)
- 1053 20. V. Bousson, A. Meunier, C. Bergot, É. Vicaut, M.A. Rocha, M.H. Morais, A.-M. Laval-Jeantet,
- 1054 J.-D. Laredo, Distribution of intracortical porosity in human midfemoral cortex by age and
- 1055 gender. *J. Bone Miner. Res.* **16**(7), 1308–1317 (2001)
- 1056 21. L. Bozec, M. Horton, Topography and mechanical properties of single molecules of type I
- 1057 collagen using atomic force microscopy. *Biophys. J.* **88**(6), 4223–4231 (2005)
- 1058 22. J. Bradley, Interactive image display for the x window system. version 3.10a, 2nd edn. (1994),
- 1059 <http://www.trilon.com/xv/manual/xv-3.10a>
- 1060 23. B. Brodsky, E.F. Eikenberry, K.C. Belbruno, K. Sterling, Variations in collagen fibril structure
- 1061 in tendons. *Biopolymers* **21**(5), 935–951 (1982)

- 1062 24. J.A. Buckwalter, M.J. Glimcher, R.R. Cooper, R. Recker, Bone biology, part I: structure, blood
 1063 supply, cells, matrix, and mineralization. *J. Bone Joint Surg.* **77-A**(8), 1256–1275 (1995)
- 1064 25. C.M. Burns, The effect of the continued ingestion of mineral acid on growth of body and bone
 1065 and on the composition of bone and of the soft tissues. *Biochem. J.* **23**(5), 860–867 (1929)
- 1066 26. A. Buxboim, I. Ivanovska, D. Discher, Matrix elasticity, cytoskeletal forces and physics of
 1067 the nucleus: how deeply do cells feel outside and in? *J. Cell Sci.* **123**(3), 297–308 (2010)
- 1068 27. D.R. Carter, W.C. Hayes, The compressive behavior of bone as a two-phase porous structure.
 1069 *J. Bone Joint Surg.* **59**(7), 954–962 (1977)
- 1070 28. K.-H. Chung, K. Bhadriraju, T.A. Spurlin, R.F. Cook, A.L. Plant, Nanomechanical properties
 1071 of thin films of type I collagen fibrils. *Langmuir* **26**(5), 3629–3636 (2010)
- 1072 29. D.M.L. Cooper, A.L. Turinsky, C.W. Sensen, Hallgrímsson, Quantitative 3D analysis of the
 1073 canal network in cortical bone by micro-computed tomography. *Anat. Rec.* **4274B**(1), 169–
 1074 179 (2003)
- 1075 30. D.M.L. Cooper, C.D.L. Thomas, J.G. Clement, A.L. Turinsky, C.W. Sensen, B. Hallgrímsson,
 1076 Age-dependent change in the 3D structure of cortical porosity at the human femoral midshaft.
 1077 *Bone* **40**, 957–965 (2014)
- 1078 31. S. Cowin, A recasting of anisotropic poroelasticity in matrices of tensor components. *Transp.*
 1079 *Porous Media* **50**, 35–56 (2003)
- 1080 32. S. Cowin, The significance of bone microstructure in mechanotransduction. *J. Biomech.* **40**
 1081 (2007)
- 1082 33. J.M. Crolet, B. Aoubiza, A. Meunier, Compact bone: numerical simulation of mechanical
 1083 characteristics. *J. Biomech.* **26**(6), 677–687 (1993)
- 1084 34. J.D. Currey, The effect of porosity and mineral content on the Young's modulus of elasticity
 1085 of compact bone. *J. Biomech.* **21**(2), 131–139 (1988)
- 1086 35. S. Cusack, A. Miller, Determination of the elastic constants of collagen by Brillouin light
 1087 scattering. *J. Mol. Biol.* **135**(1), 39–51 (1979)
- 1088 36. P. Dong, S. Hauptert, B. Hesse, M. Langer, P.-J. Gouttenoire, V. Bousson, F. Peyrin, 3D
 1089 osteocyte lacunar morphometric properties and distributions in human femoral cortical bone
 1090 using synchrotron radiation micro-CT images. *Bone* **60**, 172–185 (2014)
- 1091 37. L. Dormieux, D. Kondo, F.-J. Ulm, Microporomechanics **66**(6), 1036–1059 (2006)
- 1092 38. W.J. Drugan, J.R. Willis, A micromechanics-based nonlocal constitutive equation and esti-
 1093 mates of representative volume element size for elastic composites. *J. Mech. Phys. Solids*
 1094 **44**(4), 497–524 (1996)
- 1095 39. E. Eanes, D. Lundy, G. Marti, X-ray diffraction study of the mineralization of turkey leg
 1096 tendon. *Calcif. Tissue Int.* **6**, 239–248 (1970)
- 1097 40. L. Eberhardsteiner, C. Hellmich, Layered water in crystal interfaces as source for bone vis-
 1098 coelasticity: arguments from a multiscale approach. *Comput. Methods Biomech. Biomed.*
 1099 *Eng.* **17**(1), 48–63 (2014)
- 1100 41. A. Engler, S. Sen, H. Sweeney, D. Discher, Matrix elasticity directs stem cell lineage speci-
 1101 fication. *Cell* **126**(4), 677–689 (2006)
- 1102 42. M. Eppe, Solid-state chemical methods to investigate the nature of calcified deposits.
 1103 *Zeitschrift für Kardiologie* **390**(3) (2001)
- 1104 43. J.D. Eshelby, The determination of the elastic field of an ellipsoidal inclusion, and related
 1105 problems. *Proc. R. Soc. Lond. Ser. A Math. Phys. Sci.* **241**(1226), 376–396 (1957)
- 1106 44. A. Every, W. Sachse, Sensitivity of inversion algorithms for recovering elastic constants of
 1107 anisotropic solids from longitudinal wavespeed data. *Ultrasonics* **30**, 43–48 (1992)
- 1108 45. P. Fratzl, S. Schreiber, K. Klaushofer, Bone mineralization as studied by small-angle x-ray
 1109 scattering. *Connect. Tissue Res.* **34**(4) (1996)
- 1110 46. A. Fritsch, C. Hellmich, Universal microstructural patterns in cortical and trabecular, extra-
 1111 cellular and extravascular bone materials: micromechanics-based prediction of anisotropic
 1112 elasticity. *J. Theor. Biol.* **244**(4), 597–620 (2007)
- 1113 47. A. Fritsch, L. Dormieux, C. Hellmich, Porous polycrystals built up by uniformly and
 1114 axisymmetrically oriented needles: homogenization of elastic properties. *Comptes Rendus*
 1115 *Mécanique* **334**(3), 151–157 (2006)

- 1116 48. A. Fritsch, C. Hellmich, L. Dormieux, Ductile sliding between mineral crystals followed
1117 by rupture of collagen crosslinks: experimentally supported micromechanical explanation of
1118 bone strength. *J. Theor. Biol.* **260**(2), 230–252 (2009)
- 1119 49. H.M. Frost, Micropetrosis. *J. Bone Joint Surg.* **42**, 144–150 (1960)
- 1120 50. P. Germain, The method of virtual power in continuum mechanics. part 2: microstructure.
1121 *SIAM J. Appl. Math.* **25**(3), 556–575 (1973)
- 1122 51. J. Gong, J. Arnold, S.H. Cohn, Composition of trabecular and cortical bone. *The Anat. Rec.*
1123 **149**, 325–332 (1964)
- 1124 52. S.J. Gould, R.C. Lewontin, The spandrels of San Marco and the Panglossian paradigm: a
1125 critique of the adaptationist programme. *Proc. R. Soc. Lond. Ser. B Biol. Sci.* **205**, 581–598
1126 (1979)
- 1127 53. Q. Grimal, G. Rus, W.J. Parnell, P. Laugier, A two-parameter model of the effective elastic
1128 tensor for cortical bone. *J. Biomech.* **44**(8), 1621–1625 (2011)
- 1129 54. M. Hahn, M. Vogel, M. Pomesious-Kempa, G. Delling, Trabecular bone pattern factor a new
1130 parameter for simple quantification of bone microarchitecture. *Bone* **13**(4), 327–330 (1992)
- 1131 55. E. Hamed, Y. Lee, I. Jasiuk, Multiscale modeling of elastic properties of cortical bone. *Acta*
1132 *Mech.* **213**(1), 131–154 (2010)
- 1133 56. E. Hamed, E. Novitskaya, J. Li, I. Jasiuk, J. McKittrick, Experimentally-based multiscale
1134 model of the elastic moduli of bovine trabecular bone and its constituents. *Mater. Sci. Eng. C*
1135 **54**, 207–216 (2015)
- 1136 57. F.S. Hammet, A biochemical study of bone growth. I Changes in the ash, organics matter and
1137 water during growth (mus norvegicus albinus). *J. Biol. Chem.* **64**, 409–428 (1925)
- 1138 58. F. Hang, A.H. Barber, Nano-mechanical properties of individual mineralized collagen fibrils
1139 from bone tissue. *J. R. Soc. Interface* (2010)
- 1140 59. Z. Hashin, Analysis of composite materials a survey. *J. Appl. Mech.* **50**(3), 481 (1983)
- 1141 60. C. Hellmich, Microelasticity of Bone, in *Applied Micromechanics of Porous Materials - CISM*
1142 *Courses and Lectures*, vol. 480, ed. by L. Dormieux, F.-J. Ulm (2005)
- 1143 61. C. Hellmich, F.-J. Ulm, Micromechanical model for ultrastructural stiffness of mineralized
1144 tissues. *J. Eng. Mech.* **128**(8), 898–908 (2002)
- 1145 62. C. Hellmich, F.-J. Ulm, Are mineralized tissues open crystal foams reinforced by crosslinked
1146 collagen? – some energy arguments. *J. Biomech.* **535**(9), 1199–1212 (2002)
- 1147 63. C. Hellmich, F.-J. Ulm, Average hydroxyapatite concentration is uniform in the extracol-
1148 lagenous ultrastructure of mineralized tissues: evidence at the 1–10-microm scale. *Biomech.*
1149 *Model. Mechanobiol.* **2**(1), 21–36 (2003)
- 1150 64. C. Hellmich, F.-J. Ulm, Drained and undrained poroelastic properties of healthy and patho-
1151 logical bone: a poro-micromechanical investigation. *Transp. Porous Media* **58**(3), 243–268
1152 (2005)
- 1153 65. C. Hellmich, J.-F. Barthélémy, L. Dormieux, Mineralcollagen interactions in elasticity of bone
1154 ultrastructure a continuum micromechanics approach. *Eur. J. Mech. A/Solids* **23**(5), 783–810
1155 (2004)
- 1156 66. C. Hellmich, F.-J. Ulm, L. Dormieux, Can the diverse elastic properties of trabecular and corti-
1157 cal bone be attributed to only a few tissue-independent phase properties and their interactions?
1158 *Biomech. Model. Mechanobiol.* **2**(4), 219–238 (2004)
- 1159 67. C. Hellmich, D. Celundova, F.-J. Ulm, Multiporoelasticity of hierarchically structured materi-
1160 als: micromechanical foundations and application to bone. *J. Eng. Mech.* **135**(5), 382–394
1161 (2009)
- 1162 68. P. Helnwein, Some remarks on the compressed matrix representation of symmetric second-
1163 order and fourth-order tensors. *Comput. Methods Appl. Mech. Eng.* **190**(2223), 2753–2770
1164 (2001)
- 1165 69. A.V. Hershey, The elasticity of an isotropic aggregate of anisotropic cubic crystals. *J. Appl.*
1166 *Mech. Trans. ASME* **21**(3), 236–240 (1954)
- 1167 70. B. Hesse, P. Varga, M. Langer, A. Pacureanu, S. Schrof, N. Männicke, H. Suhonen, P. Maurer,
1168 P. Cloetens, F. Peyrin, K. Raum, Canalicular network morphology is the major determinant of
1169 the spatial distribution of mass density in human bone tissue: evidence by means of synchrotron
1170 radiation phase-contrast nano-CT. *J. Bone Miner. Res.* **30**(2), 346–356 (2015)

- 1171 71. R. Hill, Elastic properties of reinforced solids: some theoretical principles. *J. Mech. Phys.*
1172 *Solids* **11**(5), 357–372 (1963)
- 1173 72. A.J. Hodge, J.A. Petruska, Recent studies with the electron microscope on ordered aggregates
1174 of the tropocollagen molecule, in *Aspects of Protein Structure - Proceedings of a Symposium*
1175 *held in Madras 14–18 January 1963 and organized by the University of Madras, India*, ed.
1176 by G.N. Ramachandran (Academic Press, New York, 1963), pp. 289–300
- 1177 73. G.K. Hunter, P.V. Hauschka, R.A. Poole, L.C. Rosenberg, H.A. Goldberg, Nucleation and
1178 inhibition of hydroxyapatite formation by mineralized tissue proteins. *Biochem. J.* **317**(1),
1179 59–64 (1996)
- 1180 74. R. Jilka, R. Weinstein, T. Bellido, A. Parfitt, S. Manolagas, Osteoblast programmed cell death
1181 (apoptosis): modulation by growth factors and cytokines. *J. Bone Miner. Res.* **13**(5), 793–802
1182 (1998)
- 1183 75. J. Jowsey, Age changes in human bone. *Clin. Orthop.* **17**, 210–218 (1960)
- 1184 76. E.P. Katz, S.T. Li, Structure and function of bone collagen fibrils. *J. Mol. Biol.* **80**(1), 1–15
1185 (1973)
- 1186 77. J.L. Katz, K. Ukraincik, On the anisotropic elastic properties of hydroxyapatite. *J. Biomech.*
1187 **4**(3), 221–227 (1971)
- 1188 78. J.L. Katz, H.S. Yoon, S. Lipson, R. Maharidge, A. Meunier, P. Christel, The effects of remodel-
1189 ing on the elastic properties of bone. *Calcif. Tissue Int.* **36**(1), 31–36 (1984)
- 1190 79. T.M. Keaveny, E.F. Wachtel, C.M. Ford, W.C. Hayes, Differences between the tensile and
1191 compressive strengths of bovine tibial trabecular bone depend on modulus. *J. Biomech.* **27**(9),
1192 1137–1146 (1994)
- 1193 80. C. Kohlhauser, C. Hellmich, Determination of Poissons ratios in isotropic, transversely
1194 isotropic, and orthotropic materials by means of combined ultrasonic-mechanical testing of
1195 normal stiffnesses: application to metals and wood. *Eur. J. Mech. A/Solids* **33**, 82–98 (2012)
- 1196 81. C. Kohlhauser, C. Hellmich, Ultrasonic contact pulse transmission for elastic wave velocity
1197 and stiffness determination: influence of specimen geometry and porosity. *Eng. Struct.* **47**,
1198 115–133 (2013)
- 1199 82. R. Kriz, W. Stinchcomb, Elastic moduli of transversely isotropic graphite fibers and their
1200 composites. *Exp. Mech.* **19**(2), 41–49 (1979)
- 1201 83. E. Kröner, Berechnung der elastischen Konstanten des Vielkristalls aus den Konstanten des
1202 Einkristalls. *Zeitschrift für Physik* **151**(4), 504–518 (1958)
- 1203 84. N. Laws, The determination of stress and strain concentrations at an ellipsoidal inclusion in
1204 an anisotropic material. *J. Elast.* **7**(1), 91–97 (1977)
- 1205 85. N. Laws, A note on penny-shaped cracks in transversely isotropic materials. *Mech. Mater.*
1206 **4**(2), 209–212 (1985)
- 1207 86. S. Lees, Considerations regarding the structure of the mammalian mineralized osteoid from
1208 viewpoint of the generalized packing model. *Connect. Tissue Res.* **16**, 281–303 (1987)
- 1209 87. S. Lees, Mineralization of type I collagen. *Biophys. J.* **85**, 204–207 (2003)
- 1210 88. S. Lees, J. Heeley, Density of a sample bovine cortical bone matrix and its solid constituent
1211 in various media. *Calcif. Tissue Int.* **33**, 499–504 (1981)
- 1212 89. S. Lees, H.A. Mook, Equatorial diffraction spacing as a function of water content in fully
1213 mineralized cow bone determined by neutron diffraction. *Connect. Tissue Res.* **39**, 291–292
1214 (1986)
- 1215 90. S. Lees, E.A. Page, A study of some properties of mineralized turkey leg tendon. *Connect.*
1216 *Tissue Res.* **28**(4), 263–287 (1992)
- 1217 91. S. Lees, P.F. Cleary, J.D. Heeley, E.L. Garipey, Distribution of sonic plesio-velocity in a
1218 compact bone sample. *J. Acoust. Soc. Am.* **66**(3), 641–646 (1979)
- 1219 92. S. Lees, J.M. Ahern, M. Leonard, Parameters influencing the sonic velocity in compact calcified
1220 tissues of various species. *J. Acoust. Soc. Am.* **74**(1), 28–33 (1983)
- 1221 93. S. Lees, L.C. Bonar, H.A. Mook, A study of dense mineralized tissue by neutron diffraction.
1222 *Int. J. Biol. Macromol.* **6**(6), 321–326 (1984)
- 1223 94. S. Lees, D. Hanson, E.A. Page, H. Mook, Comparison of dosage-dependent effects of beta-
1224 aminopropionitrile, sodium fluoride, and hydrocortisone on selected physical properties of
1225 cortical bone. *J. Bone Miner. Res.* **9**(9), 1377–1389 (1994)

- 1226 95. S. Lees, K.S. Probst, V.K. Ingle, K. Kjoller, The loci of mineral in turkey leg tendon as seen
1227 by atomic force microscope and electron microscopy. *Calcif. Tissue Int.* **55**, 180–189 (1994)
- 1228 96. S. Lees, D. Hanson, E.A. Page, Some acoustical properties of the otic bones of a fin whale. *J.*
1229 *Acoust. Soc. Am.* **99**(4), 2421–2427 (1995)
- 1230 97. V. Lemaire, F.L. Tobin, L.D. Greller, C.R. Cho, L.J. Suva, Modeling the interactions between
1231 osteoblast and osteoclast activities in bone remodeling. *J. Theor. Biol.* **229**, 293–309 (2004)
- 1232 98. J. Martínez-Reina, J. Domínguez, J.M. García-Aznar, Effect of porosity and mineral content on
1233 the elastic constants of cortical bone: a multiscale approach. *Biomech. Model. Mechanobiol.*
1234 **210**(3), 309–322 (2011)
- 1235 99. G.A. Maugin, The principle of virtual power: from eliminating metaphysical forces to pro-
1236 viding an efficient modelling tool. *Contin. Mech. Thermodyn.* **5**(2), 127–146 (2013)
- 1237 100. R.N. McCarthy, L.B. Jeffcott, R.N. McCartney, Ultrasound speed in equine cortical bone:
1238 effects of orientation, density, porosity and temperature. *J. Biomech.* **23**(11), 1139–1143
1239 (1990)
- 1240 101. E.A. McNally, H.P. Schwarcz, A model for the ultrastructure of bone based on electron
1241 microscopy of ion-milled sections. *PLOS one* **7**(1), e29258 (2012)
- 1242 102. K.M. Meek, N.J. Fullwood, P.H. Cooke, G.F. Elliott, D.M. Maurice, A.J. Quantock, R.S. Wall,
1243 C.R. Worthington, Synchrotron X-ray diffraction studies of the cornea, with implications for
1244 stromal hydration. *Biophys. J.* **60**(2), 467–474 (1991)
- 1245 103. T.A. Metzger, T.C. Kriepke, T.J. Vaughan, L.M. McNamara, G.L. Niebur, The in situ mechan-
1246 ics of trabecular bone marrow: the potential for mechanobiological response. *J. Biomech. Eng.*
1247 **137**(1), 011006 (2015)
- 1248 104. C. Miles, M. Ghelashvili, Polymer-in-a-box mechanism for the thermal stabilization of col-
1249 lagen molecules in fibers. *Biophys. J.* **76**(6), 3243–3252 (1999)
- 1250 105. A. Miller, S.B. Parker, The organic matrix of bone. *Phil. Trans. R. Soc. B* **304**, 455–477 (1984)
- 1251 106. T. Mori, K. Tanaka, Average stress in matrix and average elastic energy of materials with
1252 misfitting inclusions. *Acta Metall.* **21**(5), 571–574 (1973)
- 1253 107. C. Morin, C. Hellmich, Mineralization-driven bone tissue evolution follows from fluid-to-
1254 solid phase transformations in closed thermodynamic systems. *J. Theor. Biol.* **335**, 185–197
1255 (2013)
- 1256 108. C. Morin, C. Hellmich, A multiscale poromicromechanical approach to wave propagation
1257 and attenuation in bone. *Ultrasonics* **54**(5), 1251–1269 (2014)
- 1258 109. C. Morin, C. Hellmich, P. Henits, Fibrillar structure and elasticity of hydrating collagen: a
1259 quantitative multiscale approach. *J. Theor. Biol.* **317**, 384–393 (2013)
- 1260 110. S. Nikolov, D. Raabe, Hierarchical modeling of the elastic properties of bone at submicron
1261 scales: the role of extrafibrillar mineralization. *Biophys. J.* **94**(11), 4220–4232 (2008)
- 1262 111. B.S. Noble, The osteocyte lineage. *Arch. Biochem. Biophys.* **473**, 106–111 (2008)
- 1263 112. J.P.R.O. Orgel, T.C. Irving, A. Miller, T.J. Wess, Microfibrillar structure of type I collagen in
1264 situ. *Proc. Nat. Acad. Sci. U. S. A.* **103**(24), 9001–9005 (2006)
- 1265 113. P.E. Palacio-Mancheno, A.I. Larriera, S.B. Doty, L. Cardoso, S. Fritton, 3D assessment of cor-
1266 tical bone porosity and tissue mineral density using high resolution μ CT: effects of resolution
1267 and threshold method. *J. Bone Miner. Res.* **29**(1), 142–150 (2012)
- 1268 114. E. Papadakis, T. Patton, Y. Tsai, D. Thompson, R. Thompson, The elastic moduli of a thick
1269 composite as measured by ultrasonic bulk wave pulse velocity. *J. Acoust. Soc. Am.* **89**(6),
1270 2753–2757 (1991)
- 1271 115. A.M. Parfitt, The physiologic and clinical significance of bone histomorphometric data, in
1272 *Histomorphometry, Techniques and Interpretation*, ed. by R.R. Recker (CRC Press Inc, Boca
1273 Raton, 1983), pp. 143–223
- 1274 116. W.J. Parnell, Q. Grimal, The influence of mesoscale porosity on cortical bone anisotropy.
1275 Investigations via asymptotic homogenization. *J. R. Soc. Interface* **6**, 97–109 (2009)
- 1276 117. F. Peters, K. Schwarz, M. Epple, The structure of bone studied with synchrotron X-ray dif-
1277 fraction, X-ray absorption spectroscopy and thermal analysis. *Thermochim. Acta* **361**(1–2)
1278 (2000)

- 1279 118. R.M.V. Pidaparti, D.B. Burr, Collagen fiber orientation and geometry effects on the mechanical
1280 properties of secondary osteons. *J. Biomech.* **25**(8) (1992)
- 1281 119. R.M.V. Pidaparti, A. Chandran, Y. Takano, C.H. Turner, Bone mineral lies mainly outside
1282 collagen fibrils: predictions of a composite model for osteonal bone. *J. Biomech.* **29**(7) (1996)
- 1283 120. S. Pradhan, D. Katti, K. Katti, Steered molecular dynamics study of mechanical response of
1284 full length and short collagen molecules. *J. Micromech. Microeng.* **1**(3), 104110 (2011)
- 1285 121. K. Probst, S. Lees, The locus of mineral crystallites in bone. *Connect. Tissue Res.* **18**(1),
1286 41–54 (1988)
- 1287 122. K.S. Probst, S. Lees, Visualization of crystal-matrix structure. In situ demineralization of
1288 mineralized turkey leg tendon and bone. *Calcif. Tissue Int.* **59**(6), 474–479 (1996)
- 1289 123. T. Qu, D. Verma, M. Shahidi, B. Pichler, Mechanics of organic-inorganic biointerfaces Implications for strength and creep properties. *MRS Bull.* **40**(4), 349–358 (2015)
- 1290 124. A.G. Reisinger, D.H. Pahr, P.K. Zysset, Sensitivity analysis and parametric study of elastic
1291 properties of a unidirectional mineralized bone fibril-array using mean field methods.
1292 *Biomech. Model. Mechanobiol.* **9**(5) (2010)
- 1293 125. J.-Y. Rho, M.E. Roy, T.Y. Tsui, G.M. Pharr, Elastic properties of microstructural components
1294 of human bone tissue as measured by nanoindentation. *J. Biomed. Mater. Res.* **45**(1), 48–54
1295 (1998)
- 1296 126. J.Y. Rho, M.C. Hobatho, R.B. Ashman, Relations of mechanical properties to density and CT
1297 numbers in human bone. *Med. Eng. Phys.* **17**(5), 347–355 (1995)
- 1298 127. R. Riedl, A systems-analytical approach to macro-evolutionary phenomena. *Q. Rev. Biol.*
1299 **52**(4), 351–370 (1977)
- 1300 128. R.A. Robinson, Chemical analysis and electron microscopy of bone, in *Bone as Tissue*, ed.
1301 by K. Rodahl, J.T. Nicholson, E.M. Brown Jr. (McGraw-Hill, New-York, 1960), pp. 186–250
- 1302 129. P.J.M. Roholl, E. Blauw, C. Zurcher, J.A.M.A. Dormans, H.M. Theuns, Evidence for a diminished
1303 maturation of preosteoblasts into osteoblasts during aging in rats: an ultrastructural
1304 analysis. *J. Bone Miner. Res.* **9**(3), 355–366 (1994)
- 1305 130. M.A. Rougvie, R.S. Bear, An X-Ray diffraction investigation of swelling by collagen. *J. Am.
1306 Leather Chem. Assoc.* **48**(12), 735–751 (1953)
- 1307 131. J. Salençon, *Handbook of Continuum Mechanics* (Springer, Berlin, 2001)
- 1308 132. V. Sansalone, S. Naili, V. Bousson, C. Bergot, F. Peyrin, J. Zarka, J.D. Laredo, G. Haiat,
1309 Determination of the heterogeneous anisotropic elastic properties of human femoral bone:
1310 from nanoscopic to organ scale. *J. Biomech.* **43**(10) (2010)
- 1311 133. N. Sasaki, S. Odajima, Stress-strain curve and Young's modulus of a collagen molecule as
1312 determined by the X-ray diffraction technique. *J. Biomech.* **29**(5), 655–658 (1996)
- 1313 134. S. Scheiner, P. Pivonka, C. Hellmich, Coupling systems biology with multiscale mechanics,
1314 for computer simulations of bone remodeling. *Comput. Methods Appl. Mech. Eng.* **254**,
1315 181–196 (2013)
- 1316 135. S. Scheiner, P. Pivonka, C. Hellmich, Mathematical modeling of postmenopausal osteoporosis
1317 and its treatment by the anti-catabolic drug denosumab. *Numer. Methods Biomed. Eng.* **30**,
1318 127 (2014)
- 1319 136. S. Scheiner, P. Pivonka, C. Hellmich, Poromicromechanics reveals that physiological bone
1320 strains induce osteocyte-stimulating lacunar pressure. *Biomech. Model. Mechanobiol.* **15**(1),
1321 928 (2016)
- 1322 137. P. Schneider, M. Stauber, R. Voide, M. Stampanoni, L.R. Donahue, R. Müller, Ultrastructural
1323 properties in cortical bone vary greatly in two inbred strains of mice as assessed by synchrotron
1324 light based micro- and nano-CT. *J. Bone Miner. Res.* **22**(10), 1557–1570 (2007)
- 1325 138. P. Schneider, M. Meier, R. Wepf, R. Müller, Serial FIB/SEM imaging for quantitative 3D
1326 assessment of the osteocyte lacuno-canalicular network. *Bone* **49**(2), 304–311 (2011)
- 1327 139. H.P. Schwarcz, E.A. McNally, G.A. Botton, Dark-field transmission electron microscopy of
1328 cortical bone reveals details of extrafibrillar crystals. *J. Struct. Biol.* **188**(3), 240–248 (2014)
- 1329 140. W.K. Sietsema, Animal models of cortical porosity. *Bone* **17**(4), 297–305 (1995)
- 1330 141. K.T. Tai, F.-J. Ulm, C. Ortiz, Nanogranular origins of the strength of bone. *Nanoletters* **6**(11),
1331 2520–2525 (2006)
- 1332

- 1333 142. N.-J. Tao, S.M. Lindsay, S. Lees, Studies of compact hard tissues and collagen by means of
1334 brillouin light scattering. *Connect. Tissue Res.* **24**(3–4), 187–205 (1990)
- 1335 143. S. Teitelbaum, Bone resorption by osteoclasts. *Science* **289**, 1504–1508 (2000)
- 1336 144. S.M. Tommasini, A. Trinward, A.S. Acerbo, F. De Carlo, L.M. Miller, S. Judex, Changes in
1337 intracortical microporosities induced by pharmaceutical treatment of osteoporosis as detected
1338 by high resolution micro-CT. *Bone* **50**, 596–604 (2012)
- 1339 145. C.H. Turner, S.C. Cowin, J.Y. Rho, R.B. Ashman, J.C. Rice, The fabric dependence of the
1340 orthotropic elastic constants of cancellous bone. *J. Biomech.* **23**(6), 549–561 (1990)
- 1341 146. M.R. Urist, R.J. DeLange, G.A. Finerman. Bone cell differentiation and growth factors. *Sci-*
1342 *ence* (1983)
- 1343 147. J. Vuong, C. Hellmich, Bone fibrillogenesis and mineralization: quantitative analysis and
1344 implications for tissue elasticity. *J. Theor. Biol.* **287**, 115–130 (2011)
- 1345 148. B.E. Warren, X-ray diffraction methods. *J. Appl. Phys.* **12**(5), 375–384 (1941)
- 1346 149. B.E. Warren, B.L. Averbach, The effect of cold-work distortion on X-ray patterns. *J. Appl.*
1347 *Phys.* **21**(6), 595–599 (1950)
- 1348 150. S. Weiner, H.D. Wagner, The material bone: structure-mechanical function relations. *Annu.*
1349 *Rev. Mater. Sci.* **28**, 271–298 (1998)
- 1350 151. S. Weiner, T. Arad, I. Sabanay, W. Traub, Rotated plywood structure of primary lamellar bone
1351 in the rat: orientations of the collagen fibril arrays. *Bone* **20**, 509–514 (1997)
- 1352 152. J. Wergedal, Baylink, Electron microprobe measurements of bone mineralization rate in vivo.
1353 *Am. J. Physiol.* **226**(2), 345–352 (1974)
- 1354 153. H.P. Wiesmann, U. Meyer, U. Plate, H.J. Hhling, Aspects of collagen mineralization in hard
1355 tissue formation. *Int. Rev. Cytol.* **242**, 121–156 (2005)
- 1356 154. Y.J. Yoon, S.C. Cowin, The estimated elastic constants for a single bone osteonal lamella.
1357 *Biomech. Model. Mechanobiol.* **7**(1) (2008)
- 1358 155. A. Zajac, D. Discher, Cell differentiation through tissue elasticity-coupled, myosin-driven
1359 remodeling. *Curr. Opin. Cell Biol.* **20**(6), 609–615 (2008)
- 1360 156. A. Zaoui, Structural morphology and constitutive behavior of microheterogeneous materials,
1361 *Continuum Micromechanics* (Springer, Berlin, 1997), pp. 291–347
- 1362 157. A. Zaoui, Continuum micromechanics: survey. *J. Eng. Mech.* **128**(8), 808–816 (2002)
- 1363 158. J.-X. Zhu, Y. Sasano, I. Takahashi, I. Mizogushi, M. Kagayama, Temporal and spatial gene
1364 expression of major bone extracellular matrix molecules during embryonic mandibular osteo-
1365 genesis in rats. *Histochem. J.* **33**, 25–35 (2001)
- 1366 159. L. Zylberberg, W. Traub, V. de Buffrenil, F. Allizard, T. Arad, S. Weiner, Rostrum of a toothed
1367 whale: ultrastructural study of a very dense bone. *Bone* **23**, 241–247 (1998)



Author Queries

Chapter 4

Query Refs.	Details Required	Author's response
AQ1	Please check and confirm if the authors and their respective affiliations have been correctly identified. Amend if necessary.	
AQ2	The citation of "Lees et al. (1992)" has been modified to "Lees and Page [90]". Please check, and correct if necessary.	

MARKED PROOF

Please correct and return this set

Please use the proof correction marks shown below for all alterations and corrections. If you wish to return your proof by fax you should ensure that all amendments are written clearly in dark ink and are made well within the page margins.

<i>Instruction to printer</i>	<i>Textual mark</i>	<i>Marginal mark</i>
Leave unchanged	... under matter to remain	Ⓟ
Insert in text the matter indicated in the margin	∧	New matter followed by ∧ or ∧ [Ⓢ]
Delete	/ through single character, rule or underline or ┌───┐ through all characters to be deleted	Ⓞ or Ⓞ [Ⓢ]
Substitute character or substitute part of one or more word(s)	/ through letter or ┌───┐ through characters	new character / or new characters /
Change to italics	— under matter to be changed	↵
Change to capitals	≡ under matter to be changed	≡
Change to small capitals	≡ under matter to be changed	≡
Change to bold type	~ under matter to be changed	~
Change to bold italic	≈ under matter to be changed	≈
Change to lower case	Encircle matter to be changed	≡
Change italic to upright type	(As above)	⊕
Change bold to non-bold type	(As above)	⊖
Insert 'superior' character	/ through character or ∧ where required	Υ or Υ under character e.g. Υ or Υ
Insert 'inferior' character	(As above)	∧ over character e.g. ∧
Insert full stop	(As above)	⊙
Insert comma	(As above)	,
Insert single quotation marks	(As above)	Ƴ or ƴ and/or ƶ or Ʒ
Insert double quotation marks	(As above)	ƶ or Ʒ and/or Ƹ or ƹ
Insert hyphen	(As above)	⊞
Start new paragraph	┌	┌
No new paragraph	┐	┐
Transpose	└┘	└┘
Close up	linking ○ characters	Ⓞ
Insert or substitute space between characters or words	/ through character or ∧ where required	Υ
Reduce space between characters or words		↑